Available online at www.sciencedirect.com
SCIENCE DIRECT®
ELSEVIER
European Journal of Mechanics B/Fluids 22 (2003) 445–471

3D numerical simulation of regular structure formation in a locally heated falling film

Alexander M. Frank

Institute of Computational Modelling SB RAS, Akademgorodok, Krasnoyarsk, 660036, Russia

Received 12 September 2002; received in revised form 24 April 2003; accepted 26 June 2003

Abstract

A thin-film flow on a locally heated vertical plate is studied numerically by solving a full 3D nonlinear time-dependent problem. The method of particles for incompressible fluid has been adapted to take into account viscous and surface tension forces. The effect of periodic rivulet-like structure formation, observed experimentally at moderate heating, has been simulated and investigated. The interesting flow picture including the spots of a strong reverse and spanwise thermocapillary surface flows is revealed. Some qualitative and quantitative comparisons with the experimental results are presented.

Keywords: Film flow; Thermocapillarity; Instability; Regular structure; Rivulets

1. Introduction

The instability of a film flow on a heated incline is being intensively studied both due to a rich physical content of the phenomenon and a great number of technological applications of the film flows. Mainly, the layers uniformly heated from below have been considered. A review of some theoretical results, concerning both linear and nonlinear effects, can be found in [1] and Introduction to [2]. In the latter paper, a mechanism for rivulets formation is proposed, based on a three-dimensional surface-wave instability coupled with thermocapillary instability.

The problem on thermocapillary instabilities in horizontal layer with a presence of horizontal or oblique temperature gradient has also received considerable attention, particularly, in connection with hydrothermal waves predicted by linear analysis [3]. The works on nonuniformly heated falling films are much more rare. To our knowledge, few theoretical studies exist in literature. In [4], the influence of streamwise temperature gradient imposed at the plate is investigated. Both linear analysis and numerical solution of the Benny-type equation, derived for the case of nonuniform heating, has been made for 2D flow. The 3D secondary instability is investigated in [5]. The paper [6] considers a sinusoidal temperature distribution at the plate. The there derived evolution equation for the film thickness accounts for two thermocapillary instability mechanisms – one connected with a heat transfer at the liquid–gas interface, and the other one with bottom temperature inhomogeneity. In particular, a special non-symmetric periodical temperature distribution was considered, and a comparison with film thickness profiles, experimentally measured in [7], was made for 2D flow, before 3D bifurcation takes place (see below).

Among experimental studies, there is a large series of papers [7–12] on investigation of films falling down a locally heated incline, when the heater is a stripe elongated in spanwise direction (only some of the papers are cited here). It was shown, that if a heating is low enough, only 2D flow with a bump at the front edge of a heater is observed. For the larger heat flux this primary flow becomes unstable, and this instability leads to another steady or quasisteady 3D flow, which looks like a regular structure with a periodically bent leading bump and longitudinal rolls or rivulets descending from it downstream, with a much thinner

E-mail address: frank@icm.krasn.ru (A.M. Frank).

0997-7546/$ – see front matter
doi:10.1016/S0997-7546(03)00056-6

liquid film between them (Fig. 13). This structure sharpens with the heat flux increase, the distance between rivulets grows, and smaller rolls appear between the main ones.

Numerical simulations of the phenomenon have been made in [6,11,13,14] using one or another thin-layer approximation, but in two dimensions only, so they could not reveal the 3D bifurcation in principle. Recently, the other attempt to simulate this phenomenon numerically has been made in [15]. There was also used some thin-layer approximation but in three dimensions already. Calculations demonstrated leading bump and edge rolls formation but a periodic structure was not obtained.

In present work, we investigate this regular structure formation via direct 3D numerical simulation. Among recent two-dimensional direct numerical simulations of film flows, using Navier–Stokes equations, are the works [16–18]. In [18], the energy equation and temperature-dependent surface tension were included, in order to describe thermocapillary instability leading to a film rupture. Later, these authors made 3D simulation [19] of thermocapillary instability leading to rivulets formation.

The paper is organized as follows. In Section 2, basic equations, boundary conditions and variational formulation of the problem are described. Section 3 presents the numerical method of particles for incompressible viscous flows with viscosity and surface tension depending on temperature. In Section 4, we give some details of numerical realization of the method. In Section 5, the two test problems are considered. Section 6 contains the main results of 3D simulations. We summarize in Section 7.

2. Problem statement

A liquid film over an inclined rigid plate is considered (Fig. 1). The flow of viscous incompressible fluid is driven by gravity and is also strongly affected by thermocapillary forces due to a local heating at the bottom. The reference frame is Cartesian with X axis along the mainstream, and Z axis normal to the plate with the origin $Z = 0$ at the plate surface. The typical initial film thickness H is 0.1 mm, computational domain width and length are 5–15 mm and 18 mm, respectively. For such a thin-film flow the buoyancy effects are negligibly small in comparison with thermocapillary ones and, hence, the fluid density ρ is assumed to be constant. This follows from the estimate for the Marangoni, Prandtl and Grashof numbers ratio $Ma/(Pr \cdot Gr)$, the value of which is in our case greater than 10^3 (see the end of the section for these numbers definition). Taking into account the results of numerical calculations [11], the viscosity μ is assumed to depend on temperature, while the variation of heat conductivity k is neglected. Thus, the flow is governed by equations

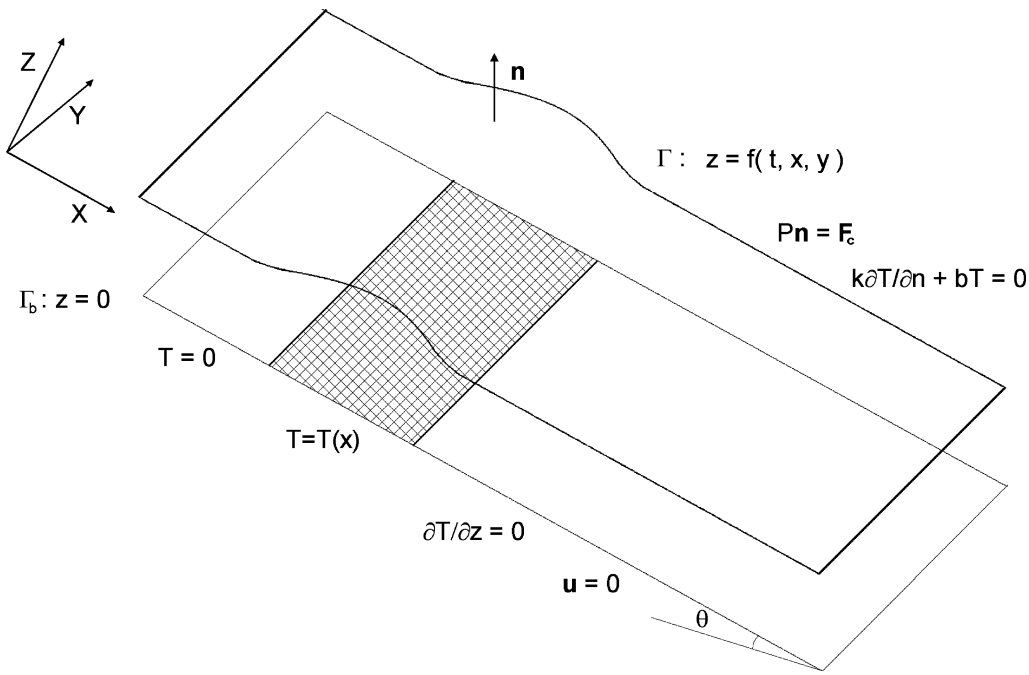

Fig. 1. Reference frame, sketch of the flow and boundary conditions at the bottom and free surface.

$$\rho\frac{\mathrm{D}\mathbf{u}}{\mathrm{D}t} = \operatorname{div} P + \rho\mathbf{g}, \tag{1}$$

$$\operatorname{div}\mathbf{u} = 0, \tag{2}$$

$$\frac{\mathrm{D}T}{\mathrm{D}t} = \kappa\nabla^2 T, \tag{3}$$

$$P = -pI + 2\mu(T)S, \tag{4}$$

$$\mathbf{F}_c = K\sigma(T)\mathbf{n} + \nabla_\Gamma\sigma(T), \tag{5}$$

$$\sigma(T) = \sigma_0 - \sigma_1 T, \tag{6}$$

$$K = \operatorname{div}_\Gamma \mathbf{n} = \operatorname{div}\mathbf{n}, \tag{7}$$

$$\nabla_\Gamma = \nabla - \mathbf{n}(\mathbf{n}\cdot\nabla), \tag{8}$$

$$\mathbf{g} = g(\sin\theta, 0, -\cos\theta). \tag{9}$$

Here $\mathrm{D}/\mathrm{D}t = \partial/\partial t + \mathbf{u}\cdot\nabla$ is the material derivative, S is the strain rate tensor, T is the difference between fluid temperature and ambient air temperature, κ is the thermal diffusivity, $\mathbf{F}_c$ is the surface stress related to the boundary condition at the deformable free surface Γ (see Fig. 1), K is the doubled mean curvature of Γ, $\mathbf{n}$ is the outward unit normal to Γ, ∇_Γ is the surface gradient and g is the gravity acceleration. The boundary conditions at the bottom and free surface are given in Fig. 1, where b is the heat transfer coefficient at the free surface. We also consider a flow to be periodic in Y direction. The inlet and outlet boundary conditions will be specified below.

To obtain the numerical method we need a variational formulation of the problem. For the sake of simplicity, we assume for a while, that region Ω occupied by fluid is infinite in XY plane. Let $\boldsymbol{\Phi}$ be a smooth, compact and divergence free function vanishing at the bottom Γ_b. Let's denote $A = \operatorname{supp}\boldsymbol{\Phi}\cap\Omega$, $\gamma = \partial A\cap\Gamma$, $(\mathbf{a},\mathbf{b}) = \int_\Omega \mathbf{a}\cdot\mathbf{b}$, then due to the well known integral theorems, boundary conditions and the symmetry of tensors P and S

$$\begin{aligned}(\operatorname{div} P, \boldsymbol{\Phi}) &= \int_A \operatorname{div}(P\boldsymbol{\Phi}) - \int_A P:\nabla\boldsymbol{\Phi} = \int_{\partial A}\mathbf{n}\cdot P\boldsymbol{\Phi} - \int_A P:\nabla\boldsymbol{\Phi}\\ &= \int_{\partial A}\boldsymbol{\Phi}\cdot P\mathbf{n} - \int_A P:\nabla\boldsymbol{\Phi} = \int_\gamma \boldsymbol{\Phi}\cdot\mathbf{F}_c - 2\int_A \mu(T)S:\nabla\boldsymbol{\Phi}\\ &= \int_\gamma \boldsymbol{\Phi}\cdot\mathbf{F}_c - \int_A \mu(T)S:\left(\nabla\boldsymbol{\Phi} + \nabla\boldsymbol{\Phi}^{\mathrm{T}}\right),\end{aligned} \tag{10}$$

where ":" denotes the scalar product of tensors. Further,

$$\begin{aligned}(\rho\mathbf{g}, \boldsymbol{\Phi}) &= \left(\rho g(\mathbf{e}_1\sin\theta - \operatorname{grad}(z-H)\cos\theta), \boldsymbol{\Phi}\right)\\ &= \rho g(\mathbf{e}_1, \boldsymbol{\Phi})\sin\theta - \rho g\cos\theta\int_A \operatorname{div}\left((z-H)\boldsymbol{\Phi}\right)\\ &= \rho g(\mathbf{e}_1, \boldsymbol{\Phi})\sin\theta - \rho g\cos\theta\int_\gamma (z-H)\mathbf{n}\cdot\boldsymbol{\Phi}.\end{aligned} \tag{11}$$

Thus, multiplying Eq. (1) by $\boldsymbol{\Phi}$ and integrating over Ω gives

$$\left(\frac{\mathrm{D}\mathbf{u}}{\mathrm{D}t}, \boldsymbol{\Phi}\right) = \int_\Gamma\left(\frac{1}{\rho}\mathbf{F}_c - g(z-H)\mathbf{n}\cos\theta\right)\cdot\boldsymbol{\Phi} + (\mathbf{e_1}, \boldsymbol{\Phi})g\sin\theta - \int_\Omega \nu(T)S:\left(\nabla\boldsymbol{\Phi} + \nabla\boldsymbol{\Phi}^{\mathrm{T}}\right). \tag{12}$$

Quite similar from Eq. (3) one can obtain

$$\left(\frac{\mathrm{D}T}{\mathrm{D}t}, \Psi\right) = -\kappa(\nabla T, \nabla\Psi) - \frac{\kappa b}{k}\int_\Gamma T\Psi \tag{13}$$

for any smooth enough compact function Ψ, vanishing in that region of a bottom, where the temperature is posed.

In order to get dimensionless equations, we use a length scale H and viscous time scale H^2/ν_0, where ν_0 is the kinematic viscosity of the liquid at the initial (ambient air) temperature. And also, a temperature scale T_m, which stands for the difference between maximum temperature at the heater and initial fluid temperature. Keeping the same notations for all the dimensionless variables, one can obtain the following dimensionless form of Eqs. (12), (13)

$$\left(\frac{\mathrm{D}\mathbf{u}}{\mathrm{D}t}, \boldsymbol{\Phi}\right) = \int_{\Gamma} \left(\mathbf{F}_c - G(z-1)\mathbf{n}\cos\theta\right)\cdot\boldsymbol{\Phi} + (\mathbf{e}_1, \boldsymbol{\Phi})G\sin\theta - \int_{\Omega} N(T)S : \left(\nabla\boldsymbol{\Phi} + \nabla\boldsymbol{\Phi}^{\mathrm{T}}\right), \tag{14}$$

$$\left(\frac{\mathrm{D}T}{\mathrm{D}t}, \Psi\right) = -\frac{1}{Pr}(\nabla T, \nabla\Psi) - \frac{Bi}{Pr}\int_{\Gamma} T\Psi, \tag{15}$$

where $N(T) = \nu(TT_m)/\nu_0$, $\mathbf{F}_c = (We - \frac{Ma}{Pr}T)K\mathbf{n} - \frac{Ma}{Pr}\nabla_{\Gamma}T$, and the dimensionless parameters are

Galileo number $G = \dfrac{gH^3}{\nu_0^2}$,

Weber number $We = \dfrac{\sigma_0 H}{\rho\nu_0^2}$,

Marangoni number $Ma = \dfrac{\sigma_1 H T_m}{\rho\nu_0\kappa}$,

Prandtl number $Pr = \dfrac{\nu_0}{\kappa}$,

Biot number $Bi = \dfrac{bH}{k}$.

The Grashof number mentioned above is $Gr = G\beta T_m$, where β is a thermal-expansion coefficient of the liquid. Below, the dimensionless variables are used, unless the units of a quantity are explicitly specified.

3. Method of particles

Method of particles for incompressible fluid has been originally suggested for inviscid flows [20] and derived directly from Gauss's "the least constraint" variational principle, rather than from Euler equations for ideal fluid. Detailed description of the method and examples of it's application to different flows with a free surface can be found in [21–25]. It's extension to viscous flows is also briefly outlined in [21]. Here we show how the method can be constructed for our case of viscous flow with surface tension as an approximation to Eqs. (14), (15).

At the instant $t = 0$ we fill up an initial fluid domain Ω_0 with a large number of material particles, each having mass m_k, position $\mathbf{r}_k$, velocity $\mathbf{u}_k$ and temperature T_k, so that these discrete functions approximate initial fields of velocity, temperature and unit density. We will also use Galerkin method for Eqs. (14), (15), and at every time-level $n + 1/2$ will find continuous velocity and temperature fields

$$\tilde{\mathbf{u}}^{n+1/2} = \sum_{\alpha}\lambda_{\alpha}^{n+1/2}\boldsymbol{\Phi}_{\alpha} + \sum_{\gamma}\bar{\lambda}_{\gamma}\boldsymbol{\Phi}_{\gamma}, \tag{16}$$

$$T^{n+1/2} = \sum_{\alpha}\eta_{\alpha}^{n+1/2}\Psi_{\alpha} + \sum_{\delta}\bar{\eta}_{\delta}\bar{\Psi}_{\delta}, \tag{17}$$

where basis functions $\boldsymbol{\Phi}_{\alpha}$, Ψ_{α} possess the same properties as $\boldsymbol{\Phi}$, Ψ, mentioned above. Second terms in (16), (17) account for the inlet velocity and bottom temperature boundary conditions, where $\bar{\lambda}_{\gamma}$, $\bar{\eta}_{\delta}$ are fixed, and functions $\bar{\Psi}_{\delta}$ do not vanish at the bottom (see below).

The main advantage of variational formulation here is that basis functions $\boldsymbol{\Phi}_{\alpha}$ and Ψ_{α} have not to satisfy any boundary conditions at the unknown free surface Γ. All these conditions for a fluid velocity and temperature are already naturally included into Eqs. (14), (15). Using the terminology of finite element methods [27], they are natural boundary conditions (as well as heat-insulation condition at the bottom), in contrast to the principle ones, like $\mathbf{u} = 0$ and $T = T(x)$ at the bottom.

Since the fluid is incompressible, one can consider the volume integrals (scalar products) in (14), (15) as being taken either in physical space over fluid region Ω, which varies in time, or in Lagrange variables $\mathbf{r}(0, \mathbf{q}) = \mathbf{q}$ over fixed region Ω_0. For any function $F(t, \mathbf{r})$ we introduce a "particle" approximation of volume integrals in (14), (15) as follows

$$[F]^{n+1/2} = \sum_{k} m_k F\left(t^{n+1/2}, \mathbf{r}_k^{n+1/2}\right) \approx \int_{\Omega_0} F\left(t^{n+1/2}, \mathbf{r}\left(t^{n+1/2}, \mathbf{q}\right)\right)\mathrm{d}q. \tag{18}$$

We also approximate free surface Γ: $z = f(t, x, y)$ at each time-level $n + 1/2$ by smoothing spline Γ_s, which is constructed on known positions of surface particles. Any surface integral $\int_{\Gamma_s} F$ then can be approximated using one or another quadrature

formula, and we denote this approximation by $\{F\}^{n+1/2}$ (in all the computations described below the cubic spline and rectangle rule have been used). Then the following numerical scheme for Eqs. (14), (15) can be employed

$$\mathbf{r}_k^{n+1/2} = \mathbf{r}_k^n + \frac{\tau}{2}\mathbf{u}_k^{n-1/2}, \tag{19}$$

$$\sum_k m_k \frac{T_k^{n+1} - T_k^n}{\tau}\Psi_\alpha\big(\mathbf{r}_k^{n+1/2}\big) = -\frac{1}{Pr}[\nabla T \cdot \nabla\Psi_\alpha]^{n+1/2} - \frac{Bi}{Pr}\{T\Psi_\alpha\}^{n+1/2}, \tag{20}$$

$$\sum_k m_k \frac{\mathbf{u}_k^{n+1/2} - \mathbf{u}_k^{n-1/2}}{\tau} \cdot \boldsymbol{\Phi}_\alpha\big(\mathbf{r}_k^{n+1/2}\big) = \big\{\big(\mathbf{F}_c - G(z-1)\mathbf{n}\cos\theta\big)\cdot\boldsymbol{\Phi}_\alpha\big\}^{n+1/2} + [\mathbf{e_1}\cdot\boldsymbol{\Phi}_\alpha]^{n+1/2} G\sin\theta - 2\big[N(T)S : S_\alpha\big]^{n+1/2}, \tag{21}$$

$$\mathbf{u}_k^{n+1/2} = \tilde{\mathbf{u}}^{n+1/2}\big(\mathbf{r}_k^{n+1/2}\big), \tag{22}$$

$$T_k^{n+1} = 2T^{n+1/2}\big(\mathbf{r}_k^{n+1/2}\big) - T_k^n, \tag{23}$$

$$\mathbf{r}_k^{n+1} = \mathbf{r}_k^n + \tau\mathbf{u}_k^{n+1/2}, \tag{24}$$

where $S_\alpha = \frac{1}{2}(\nabla\boldsymbol{\Phi}_\alpha + \nabla\boldsymbol{\Phi}_\alpha^{\mathrm{T}})$.

Substituting (22), (23) into (20), (21), with the use of (16), (17), one obtains two linear algebraic systems for the unknown coefficients in decompositions (16), (17)

$$A^{n+1/2}\lambda^{n+1/2} = F_1^{n+1/2}, \tag{25}$$

$$B^{n+1/2}\eta^{n+1/2} = F_2^{n+1/2}. \tag{26}$$

Here $\lambda^{n+1/2}$, $\eta^{n+1/2}$ denote the vectors composed by all the $\lambda_\alpha^{n+1/2}$ and $\eta_\alpha^{n+1/2}$, respectively. Matrices A and B have the components

$$A_{\alpha\beta}^{n+1/2} = [\boldsymbol{\Phi}_\alpha\cdot\boldsymbol{\Phi}_\beta]^{n+1/2} + 2\tau\big[N(T)S_\alpha : S_\beta\big]^{n+1/2}, \tag{27}$$

$$B_{\alpha\beta}^{n+1/2} = [\Psi_\alpha\Psi_\beta]^{n+1/2} + \frac{\tau}{2Pr}[\nabla\Psi_\alpha\cdot\nabla\Psi_\beta]^{n+1/2} + \frac{\tau Bi}{2Pr}\{\Psi_\alpha\Psi_\beta\}^{n+1/2}. \tag{28}$$

Thus, the numerical algorithm at each time step looks as follows. First, intermediate particle positions are found from predictor (19). Then, matrices and right-hand sides in (25), (26) are calculated, and these systems are solved to find $\lambda^{n+1/2}$, $\eta^{n+1/2}$. Finally, new continuous fields $\tilde{\mathbf{u}}^{n+1/2}$, $T^{n+1/2}$ and new particle positions, velocities and temperatures are calculated from (16), (17), (22)–(24).

The method has a simple physical interpretation. Let's consider first an inviscid flow without gravity and surface tension. Among all of the divergence free velocity fields (16) we find from (21) that one, which gives fluid particles acceleration orthogonal to all the solenoidal basis functions. It can be easily shown [21] that this results in finding the divergence free field (16) which is the closest to the free motion velocity field in some discrete L_2 norm. On the one hand, this is exactly what the Gauss's principle of "the least constraint" states [28]. On the other hand, this method can be interpreted as a free motion of particles with subsequent projection (correction) of the velocity field onto some finite-dimensional subspace of solenoidal functions. The similar procedure is well known in fractional step finite-difference schemes for the Navier–Stokes equations [29].

It has been shown [21] that the scheme (19)–(24) without gravity, surface tension and viscosity conserves momentum, is dissipative and unconditionally stable. For the initial-boundary value problem for the Navier–Stokes equations in compact region, the convergence for the solutions of (19)–(24) has been proved recently [26]. The second-order accurate time discretization, which conserves the energy exactly has also been constructed [21]. But it showed practically no advantage for the problem under consideration due to the reasons discussed below. It is still important that Eq. (24) for the particle motion in given divergence free velocity field is of second-order accuracy, because it is responsible for the residual in incompressibility constraint $|\partial\mathbf{r}/\partial\mathbf{q}| = 1$. The point is, that we calculate fluid acceleration in Lagrange variables, but the forces in Euler variables, and (24) accounts for the transformation from former to latter ones.

Thus, the method is a kind of combination of Galerkin's method with convective transport of quantities by particles. The use of particles gives a simple and convenient way of free surface tracking. A conservative combination of particle approach and Galerkin's approach allowed, on the one hand, to obtain accurate numerical solutions with very few basis functions for the smooth flows like regular surface waves, and, on the other hand, to simulate by the same method a complicated phenomenon of a rigid ball suspension by a thin liquid jet, where a free surface has a quite irregular shape [21]. Galerkin's approach, as it was

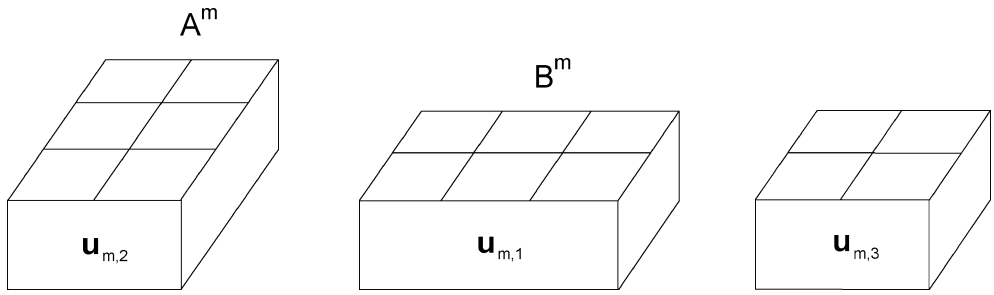

Fig. 2. Supports of compact basis functions.

shown above, permits also to take quite naturally into account viscous and surface tension forces, which act on a flow due to the corresponding additional terms in matrix and right-hand side in (25).

The general scheme of the method described above leaves a certain freedom in choosing basis functions $\boldsymbol{\Phi}_\alpha,\ \Psi_\alpha$. For the problem under consideration they have been chosen in the following way. We need functions $\boldsymbol{\Phi}_\alpha$ to be solenoidal and vanishing at the bottom, so it is quite convenient to use a vector potential. It can be shown (see Appendix A) that for the problem in half-space $z \geqslant 0$ a vector potential $\boldsymbol{\Theta}$ can always be found as

$$\boldsymbol{\Theta} = (A, B, 0), \qquad A = A_z = B = B_z = 0 \quad \text{at } z = 0. \tag{29}$$

Thus, only two it's components, satisfying certain boundary conditions, are needed in order to present any solenoidal vector field $\mathbf{u},\ \mathbf{u} = 0$ at $z = 0$, in the form

$$\mathbf{u} = \operatorname{rot} \boldsymbol{\Theta}. \tag{30}$$

Therefore, we should construct functions $\boldsymbol{\Theta}_\alpha$ of the type (29), and then (30) provides us with basis functions $\boldsymbol{\Phi}_\alpha$. In order to minimize calculations of matrices and right-hand sides in (25)–(26), the basis functions should be compact with minimal support. More exactly, the fewer is the number of functions not equal to zero at a given point (particle), the less computing time is needed to calculate matrices A and B, and the more sparce the latter are. The most appropriate smooth compact functions seem to be B-splines. As far as the thickness of the film flow is much smaller then typical streamwise and spanwise scales, it is worth choosing here $\boldsymbol{\Theta}_\alpha$ to be B-splines in $X,\ Y$ directions and polynomials in Z direction. It is also convenient to construct two-dimensional B-splines on a rectangular grid, because they become then just the product of one-dimensional B-splines.

Let multiindex $m = (i, j, l)$, where (i, j) is the node number of rectangular grid, l is the number of polynomial. We choose

$$A^m = L_i^1(x) L_j^2(y) \frac{z^{l+1}}{(l+1)!}, \qquad B^m = L_i^2(x) L_j^1(y) \frac{z^{l+1}}{(l+1)!},$$

where $L_i^1(x),\ L_i^2(x)$ are one-dimensional B-splines at the node i of the first and second order respectively (Fig. 2). Then, for every m there are two independent solenoidal basis functions

$$\boldsymbol{\Phi}_{m,1} = \left(0, A_z^m, -A_y^m\right), \qquad \boldsymbol{\Phi}_{m,2} = \left(-B_z^m, 0, B_x^m\right),$$

i.e., in the formulae (16), (21), (27) subscripts α, β mean multiindex $(m, s),\ s = 1, 2$. Basis functions $\Psi_\alpha,\ \bar{\Psi}_\alpha$ have been taken as the products of the first-order B-splines with respect to X and Y, and polynomials with respect to Z.

4. Numerical details, strain rate tensor simplification and boundary conditions

Here we describe some peculiarities of method realization, which allow to decrease computing time. It was mentioned above, that the time for matrix A computation depends on compactness of basis functions supports. This time is crucial because in 3D case it is up to 80–90% of the total computing time at each time step. There has been used a procedure, which allows to reduce this time twice for the case of chosen above basis functions and in about four times for the 3D B-splines. The procedure is based on the property of B-spline of n-th order, that is, it's derivative is a linear combination of B-splines of the order $n - 1$.

Let us introduce functions (Fig. 2)

$$\tilde{u}_m = B_z^m, \qquad \tilde{v}_m = A_z^m, \qquad \tilde{w}_m = L_i^1(x) L_j^1(y) \frac{z^{l+1}}{(l+1)!},$$
$$\mathbf{u}_{m,1} = (\tilde{u}_m, 0, 0), \qquad \mathbf{u}_{m,2} = (0, \tilde{v}_m, 0), \qquad \mathbf{u}_{m,3} = (0, 0, \tilde{w}_m),$$

then our basis functions can be represented as

$$\boldsymbol{\Phi}_{m,1} = \mathbf{u}_{m,2} - (\mathbf{u}_{m,3} - \mathbf{u}_{i,j+1,l,3})/h_y, \qquad \boldsymbol{\Phi}_{m,2} = -\mathbf{u}_{m,1} + (\mathbf{u}_{m,3} - \mathbf{u}_{i+1,j,l,3})/h_x, \tag{31}$$

where h_x and h_y are mesh sizes in X and Y directions.

Let $\boldsymbol{\Phi}$ and $\mathbf{U}$ denote vectors composed by all the $\boldsymbol{\Phi}_\alpha$ and $\mathbf{u}_\alpha$, respectively, then

$$\boldsymbol{\Phi} = D\mathbf{U},$$

where very sparce matrix D is determined by (31). It is easy to see now, that system (25) can be rewritten in the form

$$D\tilde{A}^{n+1/2}D^{\mathrm{T}}\lambda^{n+1/2} = D\widetilde{F}^{n+1/2}, \tag{32}$$

where matrix $\tilde{A}$ has the components

$$\tilde{A}^{n+1/2}_{\alpha\beta} = [\mathbf{u}_\alpha \cdot \mathbf{u}_\beta]^{n+1/2} + 2\tau\big[N(T)\widetilde{S}_\alpha : \widetilde{S}_\beta\big]^{n+1/2}. \tag{33}$$

Since the scalar product of the functions $\mathbf{u}_{m,s},\ \mathbf{u}_{m,p}$ vanishes when $s \neq p$, the first term in (33) is much easier to calculate than that one in (27). The same is true for the tensors $\widetilde{S}_\alpha, \widetilde{S}_\beta$ scalar product if a common thin-layer approximation for the strain rate tensor is used

$$\widetilde{S}_\alpha = \frac{1}{2}\big(\nabla\mathbf{u}_\alpha + \nabla\mathbf{u}_\alpha^{\mathrm{T}}\big) \approx \frac{1}{2}\begin{pmatrix} 0 & 0 & \partial u^1_\alpha/\partial z \\ 0 & 0 & \partial u^2_\alpha/\partial z \\ \partial u^1_\alpha/\partial z & \partial u^2_\alpha/\partial z & 0 \end{pmatrix}, \tag{34}$$

where $u^1_\alpha,\ u^2_\alpha$ are the X and Y components of vector $\mathbf{u}_\alpha$. The last simplification is not very principle and can be avoided, but the use of (34) provides a more sparce matrix $\tilde{A}$ and substantially simplifies the logic of the code. Below we show that the error induced by this approximation is small for the considered problem, and therefore it was used in all the 3D computations throughout this paper. The system (32) also requires less operation count than (27) if the conjugate gradients method is used and, therefore, calculations are reduced to subsequent multiplication of matrices D^{T}, $\tilde{A}$, D by some vector.

The second technique in accelerating computations is matrix $\tilde{A}$ "freezing". The specific feature of the problem is that it has two different velocity scales. The first one $U_0 = (G\sin\theta)/2$, which is the maximum inlet velocity, characterizes the mainstream and velocities caused by thermocapillary effects, which are of the same order. And the second one is a phase speed of the shortest surface capillary waves $C = (We \cdot k\tanh k)^{1/2}$, where $k = \pi/\min\{h_x, h_y\}$. In a flow under consideration, C is much larger than U, and the Courant stability condition based on a speed C requires very small time step, much smaller that the one which could be chosen from the accuracy reasons. A completely implicit scheme could help here, but the construction and numerical realization of it seem, so far, to be rather complicated due to the sophisticated dependence of surface tension force on particles coordinates. So far, the explicit scheme described above was used, but in some specific way. Since the matrix $\tilde{A}$ in (32) depends only on slow changing particle positions, unlike the right-hand side $\widetilde{F}$, which depends on fast changing surface tension forces, matrix $\tilde{A}$ can be calculated once and then fixed for several subsequent time steps. Temperature field T, also slow varying, was updated together with matrix $\tilde{A}$. Procedure like this is known in implicit stiff ODE solvers, and it allowed to speed up present computations greatly (about 5 times in average). Due to the small time steps, the second order time discretization mentioned above did not give any noticeable advantage.

The following inlet

$$u = \frac{G\sin\theta}{2}\big(2z - z^2\big), \quad v = w = 0, \quad T = 0, \quad f_x = f_{xx} = 0$$

and outlet

$$u_x = v = w = 0, \quad T_x = 0, \quad f_x = f_{xx} = 0$$

boundary conditions have been used. The inlet velocity field corresponds to Nusselt flow and it was realized by explicit assigning coefficients $\bar{\lambda}_\gamma$ in (16), as well as assigning $\bar{\eta}_\delta$ in (17) sets the temperature distribution at the bottom. The outlet boundary conditions, as well as the conditions for f are held due to the choice of special boundary splines, satisfying these restrictions exactly.

5. Test problems

First, a comparison with a well-known experiment by P. Kapitza and S. Kapitza [30] has been made. They investigated plane capillary waves in the films of water or alcohol, falling down the smooth surface under gravity. Their results have been

often used for a comparison with numerical calculations (see [16,17]). Here we have chosen a regime with "solitary" waves of the highest amplitude in alcohol film (snapshot 18 in [30]). The results of wave amplitude and shape comparison for the fixed wavelength λ and mean flow rate Q are given in Fig. 3. For the sake of simplicity, a temporal growth of a small disturbances was simulated, similar to [16,17], rather than spatial development of the wave regime studied in experiment. The calculations were conducted in a domain with periodicity boundary conditions and the length λ, corresponding to the wavelength 2.2 cm reported in [30] for this particular regime. All the necessary properties of the liquid have been also taken from that paper. An initial disturbance

$$f(0,x) = 1 + 0.05\cos(2\pi x/\lambda)$$

was imposed on the free surface, which grew then in time and led to a practically stationary wave regime. Since the mean flow rate is not constant in time due to the onset of wave motion, an initial film thickness H was selected in order to get at the stationary regime the same mean flow rate value $Q = 0.204\ \mathrm{cm}^2 \cdot \mathrm{s}^{-1}$, that was observed in experiment. The calculated phase speed of the waves appeared to be $28.3\ \mathrm{cm} \cdot \mathrm{s}^{-1}$, which is somewhat larger than measured value $26.4\ \mathrm{cm} \cdot \mathrm{s}^{-1}$. Previous calculations [16,17] also gave phase speed larger than experimental value.

As a second test, the problem on thermocapillary instability from [18,19] has been solved. The flow in a thin horizontal fluid layer heated from below is considered. The temperature at the bottom is constant $T = 1$, viscosity is also assumed to be constant. In equilibrium state, a free surface is flat and a temperature distribution across the layer is linear and determined by Biot number value. At $t = 0$ a disturbance of the form

$$f(0,x,y) = 1 + 0.1\cos(kx) + 0.1\cos(ky) \tag{35}$$

is imposed on the free surface, and a temporal evolution of the flow is studied in a domain with dimensions $\frac{2\pi}{k} \times \frac{2\pi}{k}$ and periodicity boundary conditions. First, the 2D case has been considered (no disturbance with respect to y in (35)). The resulting free surface curves at $t = 1200$ for two different resolutions are shown in Fig. 4. The following notations are used in this figure

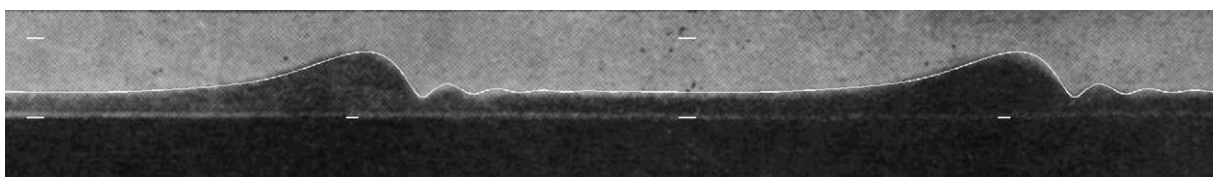

Fig. 3. First test problem. Comparison of calculated waves (white solid line) with experiment [30].

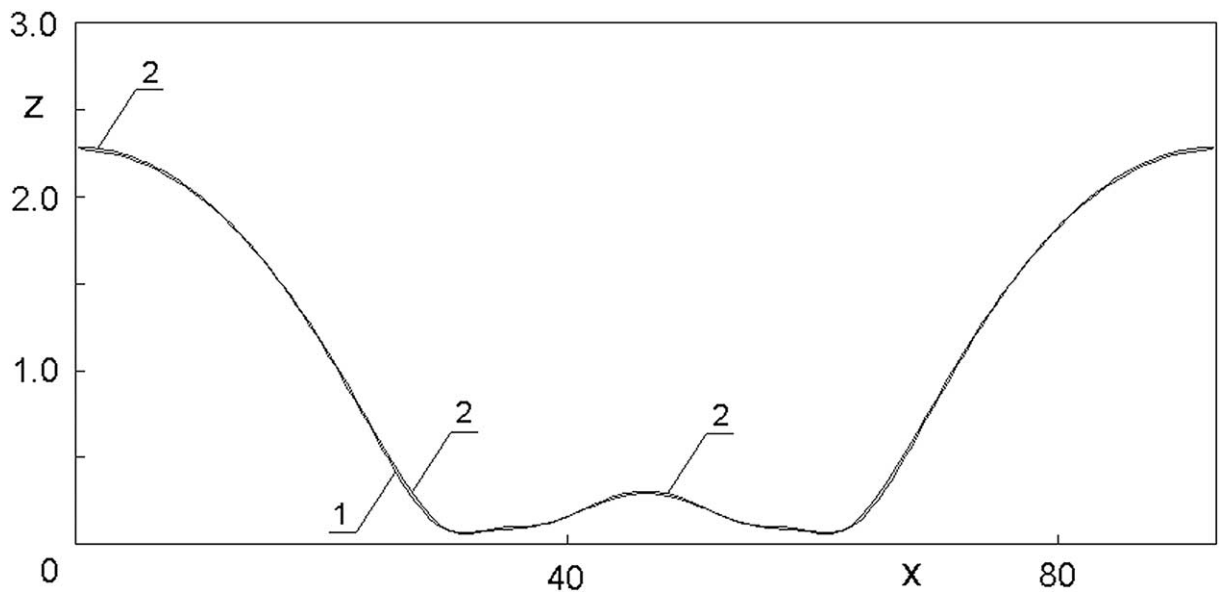

Fig. 4. Second test problem (2D case). Free surface at $t = 1200$, $G = 1$, $We = 300$, $Pr = 7.02$, $Ma = 70.2$, $Bi = 1$, $k = 0.0677$ for two different resolutions: curve 1: $m = 30$, $p = 2$, $N = 1324$; curve 2: $m = 60$, $p = 2$, $N = 3910$ (coincides with corresponding curve for the 129×11 grid from [19]).

and below: m and n are the numbers of mesh cells in X and Y directions, respectively, p is the maximum degree of polynomials with respect to Z variable, N is the number of particles in computational domain. The further increase of resolution up to $m = 120,\ p = 4,\ N = 10390$ provides graphically indistinguishable change to the curve 2, which, in it's turn, is graphically indistinguishable from the corresponding curve given in [19] (Fig. 3) for the finest 129×11 grid used there. Both 2D test problems have been calculated using the complete strain rate tensor. The use of it's simplified form (34) for the first problem (traveling waves) gives a distinct increase in waves amplitude, especially for the small ripples in front of the main wave. For the second problem, it leads to a small (about 1.5% in C norm) change to the free surface curve.

Fig. 5 demonstrates the results of calculations in 3D case. The free surface picture and the isolines of surface elevation in comparison with calculations [19] (Fig. 7(k), the final time level) are given. The agreement is very good in spite of the use of approximation (34) in present calculations. It is shown in [19] that thin-layer approximation of Benny type is not valid any more at these time values. On the contrary, the described numerical model works well here even for $p = 2$.

6. Results

All the calculations described below have been made for the 25% ethyl-alcohol water solution. The liquid properties have been taken from [6,31]. The values of the constants at the initial fluid temperature 20 °C are: density $\rho = 961.6\ \mathrm{kg \cdot m^{-3}}$, surface tension $\sigma_0 = 35.53 \times 10^{-3}\ \mathrm{N \cdot m^{-1}}$, surface tension variation with temperature $\sigma_1 = 0.1103 \times 10^{-3}\ \mathrm{N \cdot m^{-1} \cdot K^{-1}}$, heat conductivity $k = 0.4786\ \mathrm{W \cdot m^{-1} \cdot K^{-1}}$, Prandtl number $Pr = 21.8$. The dynamic viscosity is the following function of temperature

$$\mu(\widetilde{T}) = \big(6.22637 - 0.35072\widetilde{T} + 0.0131025\widetilde{T}^2 - 3.50282 \times 10^{-4}\widetilde{T}^3 + 6.07187 \times 10^{-6}\widetilde{T}^4 - 5.84788 \times 10^{-8}\widetilde{T}^5 + 2.33004 \times 10^{-10}\widetilde{T}^6\big) \times 10^{-3}\ \mathrm{kg \cdot m^{-1} \cdot s^{-1}}, \tag{36}$$

where $\widetilde{T}$ is dimensional fluid temperature (centigrade scale).

The main difficulty in simulating experiments [7–12] is that temperature distribution on heater and substrate surface is unknown. For the majority of the data only the mean heat flux determined by a power input to the heater is given. Numerical simulations [13,32] and direct temperature and heat flux measurements [12,33] show that neither constant temperature nor constant heat flux is satisfactory approximation in case of Reynolds number of order 1, at which the most distinctive periodic structures are observed. Therefore, in recent numerical calculations different approaches have been applied. In [11], the heat equation was solved in heater and fluid regions with the fixed Nusselt velocity distribution. The heat flux distribution found at the bottom was used then to calculate the surface elevation for 2D flow. In [6], also in 2D case, some model step-wise temperature distribution with smoothed front was used. The smoothing parameter was selected in order to fit the curves of surface elevation to the experimentally measured ones. In [15], a three-dimensional flow was considered using a thin-layer approximation and just constant heat flux condition was imposed. The most consistent approach would be, of course, to solve a fully coupled problem, i.e., to solve the heat equation in a heater-fluid region together with fluid dynamics equations in a flow region. But it is more complicated and, moreover, is unlikely worth doing at present for the reasons discussed in Section 7. Therefore, in this paper we apply an approach similar to that used in [6].

For the comparison, the experimental results from [11] have been chosen. Only a flow on a vertical plate is considered, i.e., $\theta = \pi/2$. The initial film thickness is fixed $H = 100$ μm. Thus, Galileo number $G = 1.511$ and Weber number $We = 569.7$ are also fixed. The Reynolds number used in [11] is $Re = G/3 \approx 0.5$. The maximum dimensionless inlet velocity $U_0 = 0.755$. The temperature distribution along a heater has been chosen in the form (see Fig. 6)

$$T(x) = 1 - \big(1 - \big((x - x_0)/L + \delta\big)/(1 + \delta)\big)^{\gamma}, \quad x_0 - \delta L \leqslant x \leqslant x_0 + L, \tag{37}$$

where x_0 is the coordinate of a heater front edge, L is a heater length, δ and γ are parameters to be determined. Dimensionless length of the heater in [11] was $L = 67$ and it's span was by an order of magnitude greater. The Biot number has been estimated there to be of the order 10^{-2}–10^{-3}. Therefore, in numerical calculations, a heat transfer between fluid and ambient air is first neglected. The influence of Biot number is studied later.

The values of parameters δ and γ have been selected by means of fitting the calculated curves of surface elevation to the experimental ones measured at the small heat flux, when only 2D flow is realized. The parameter γ affects mainly the maximum temperature gradient, and hence the amplitude and the steepness of the bump front, while δ accounts for a shift of the bump profile with respect to a heater. For every calculation, a Marangoni number value has been set, and a heat flux (local and mean) from the heater has been determined a posteriori, via direct calculation of temperature gradient at the bottom. The results of comparison for $\delta = 0.1075$, $\gamma = 6$ are plotted in Fig. 7. The distance along the heater is normalized by dimensionless capillary length $l_\sigma = \sqrt{\sigma_0/(\rho g H^2)} = \sqrt{We/G} = 19.4$. The mean heat flux values in calculations and experiment are equal.

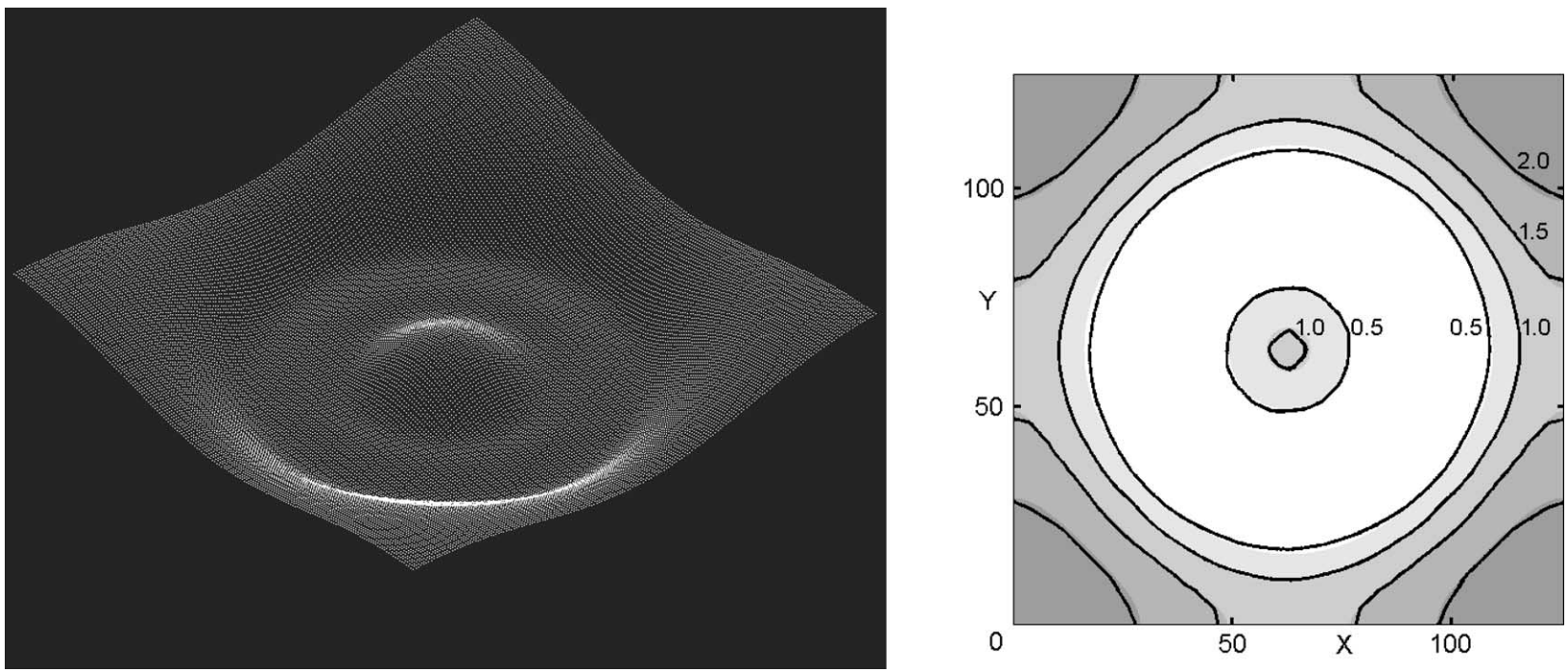

Fig. 5. Second test problem (3D case). Free surface picture (left) and isolines of the free surface elevation (right) at $t = 1242$, $G = 1$, $We = 300$, $Pr = 7.02$, $Ma = 70.2$, $Bi = 1$, $k = 0.05$, $m = n = 30$, $p = 2$, $N = 131084$. Isolines: the borders between grey shades – present work, solid lines – [19].

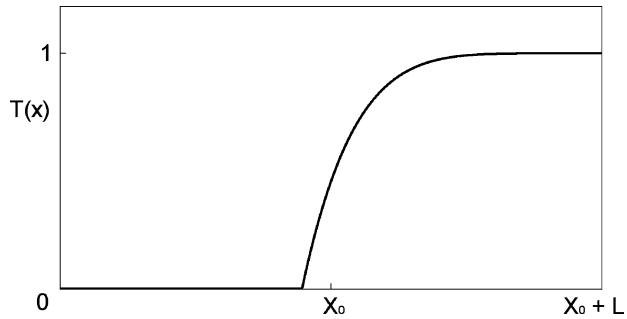

Fig. 6. Dimensionless temperature profile at the bottom, $\delta = 0.1075$, $\gamma = 6$, x_0 is the coordinate of a heater front edge and L is a heater length.

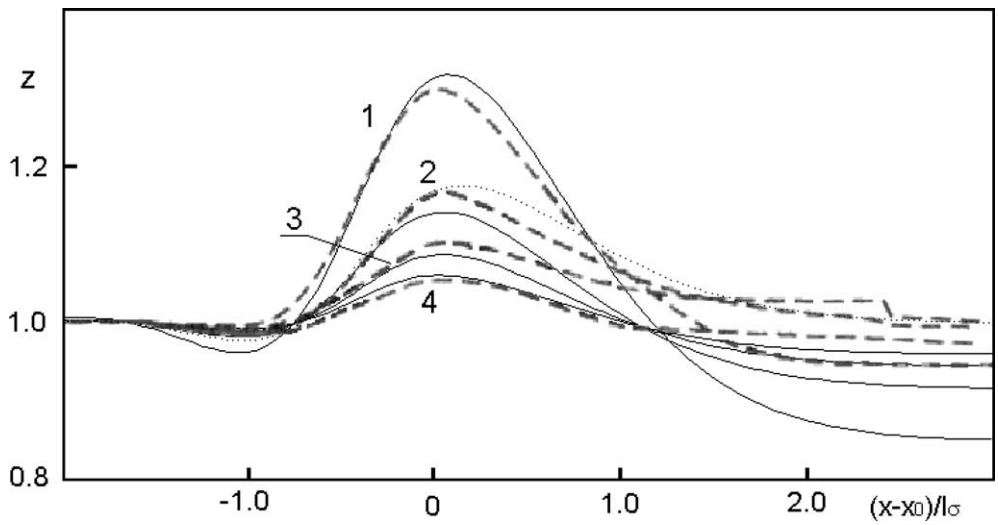

Fig. 7. Comparison of the free surface elevation profiles at $Re = 0.5$ ($Bi = 0$) for different heat flux q values. Dash lines – experiment [11], solid lines – present calculations: 1: $q = 1.21$ W · cm^{-2} ($Ma = 529$); 2: $q = 0.63$ W · cm^{-2} ($Ma = 273$); 3: $q = 0.41$ W · cm^{-2} ($Ma = 177$); 4: $q = 0.3$ W · cm^{-2} ($Ma = 127$). Ma and Bi values are the characteristics of calculations only. Dotted line 2 – calculation with constant viscosity. Dimensionless capillary length $l_\sigma = 19.4$.

The agreement between the experimental and computed curves is satisfactory and, at least, not worse than that in [6,11]. It is interesting, that for curves calculated in [11], their decreasing downstream branches are also much below the experimental profiles at $Re = 0.5$ and $Re = 2$. The agreement between these branches of profiles in [6] for different Reynolds numbers is also much worse than that for the fronts of the curves. The reason for this discrepancy is not clear yet. Some accumulating error due to numerical integration of the measured free surface slope is mentioned in [6] as one of the possible reasons. The absence of the temperature-viscosity dependence is named, as the other reason, but this dependence has been taken into consideration both in [11] and present calculations. It should be noted, that calculation with constant viscosity gives sometimes much better agreement between the curves (dotted line 2 in Fig. 7). Anyway, a temperature distribution along heater in all the discussed numerical simulations is just an approximation to a temperature distribution in real experiment, and accuracy of this approximation is not evaluated yet. Unknown heat transfer at the substrate and free surface can also give some change to a free surface shape. All this needs further investigation both experimentally and theoretically.

We also tried to check the temperature difference corresponding to the found values of Marangoni number. There is no such experimental data published either in [11] or in [7], where the experiments with the same heater and liquid are described. Only in [6] it has been mentioned, that the temperature difference in experiments at the onset of 2D bump instability was of order 10K. In our calculations (see below) this magnitude was 12K. In earlier experiments [8] with the same liquid but different heater, the direct measurements of surface temperature by an infrared scanner has been made. The typical temperature difference for the developed 3D structures, at the smallest $Re = 2$ considered in [8], was about 15K, which is also the case with our calculations, though for $Re = 0.5$ (see below).

Table 1
Some dimensionless quantities calculated with resolution refinement at $Ma = 771$ (see also caption to Fig. 8 for an explanation). Here $H_{\max}$ is the maximum film thickness, $U_{\max}$ and $U_{\min}$ are maximum and minimum streamwise velocity values, $U_0 = 0.755$ is the maximum inlet velocity (dimensionless), q is the mean heat flux, $q_* = 1.719\ \mathrm{W}\cdot\mathrm{cm}^{-2}$

Variant	$H_{\max}$	$U_{\max}/U_0$	$U_{\min}/U_0$	q/q_*
I	1.490	1.291	−0.248	1.014
II	1.506	1.272	−0.345	1.000
III	1.510	1.271	−0.344	1.000
IIs	1.510	1.273	−0.354	1.000

Small shift of temperature profile upstream, outside the heater region (see Fig. 6), seems to be quite justified due to a heat conduction in liquid and substrate. Direct temperature measurements for a film flow over a large heater [33] show, that temperature at x_0 can reach about a half of maximum heater temperature at $Re = 2.4$. Thus, all the discussed above gives a ground to consider the temperature distribution (Fig. 6) realistic enough to proceed to the further study and comparison. We used this temperature profile in all the calculations described below.

The further increase in a heat flux leads to a bump height increase, and a reverse thermocapillary flow near the bump crest appears. Fig. 8 shows the streamlines near the free surface for the 2D steady state flow calculated with different resolution. These pictures evidently demonstrate convergence. Comparison of some characteristic quantities is given in Table 1. It can be seen also, that the use of approximation (34) causes a very small change to the flow field.

The existence of a reverse flow near the crest of the bump has been foreseen in [10], and then it was simulated numerically in 2D case, using a thin-layer approximation [13]. Below we show that the magnitude of the reverse flow greatly increases in 3D case. In fact, the bump shown in Fig. 8 is highly unstable with respect to spanwise disturbances. Therefore, it can be observed in 3D calculations only for a short period of time, and then another 3D steady rivulet-like flow is realized. In Fig. 9 the snapshots of film surface show the process of this instability and 3D structure formation. Abrupt heating leads first to fast surface deformations, which then break up and are fetched down the stream, and the only steady 2D bump remains. Then, quite soon, the 3D structure appears due to an instability.

The characteristic width of a structure Λ, i.e., the distance between longitudinal rolls, must be evidently affected by computational domain width L_y due to the periodicity boundary conditions. The calculations showed that this dependence is as follows. When L_y is within some limits L_1 and L_2, where L_2 is approximately equal to $2L_1$ and L_1 depends on Marangoni number, then only one period of structure is realized. Further enlargement of L_y leads already to two periods of structure in computational domain, and this transition is rather abrupt. For example, the structure in Fig. 9 ($L_y = 150$) has exactly three periods, not one or two, though no artificial disturbances have been introduced. Moreover, the amplitude of steady state spanwise free surface deformation depends on L_y. All this is apparent evidence of preferred mode existence, and namely this mode is most likely to be observed in experiments [11] with a heater, the span of which is much greater than a structure width.

To study this preferred mode, a direct investigation of 2D bump stability has been made. At $t = 0$, a small initial disturbance of the form

$$u = u(x, z)\bigl(1 + 0.05\cos(2\pi y/L_y)\bigr)$$

is imposed on a longitudinal velocity of previously calculated steady state 2D flow, and a temporal evolution of the amplitude of spanwise free surface deformation is then studied. For every *Ma* value, several calculations with different L_y are made. Then, three of them, including that with maximum growth rate of amplitude, are used to determine the wavelength Λ_* of the most rapidly growing mode by means of parabolic interpolation. The critical value of Marangoni number $Ma_c = 466$ at $Bi = 0$ has been also found, below which all the disturbances decay. The curves for Λ_* as function of *Ma* for $Bi = 0$ and $Bi = 0.1$ are plotted in Fig. 10. They display, first, that Λ_* grows with *Ma*. Second, a large enough heat transfer at the free surface results in Λ_* decrease of just about 3–6%. Note, that $Bi = 0.1$ is, at least by one order, greater than that estimated in [11]. As far as the height of the bump also diminishes with *Bi* increase (Fig. 11), it is worth plotting Λ_* against bump height to see whether the influence of *Bi* value will diminish. Fig. 12 demonstrates this dependence, and Λ_* variation with *Bi* becomes about 3%. Therefore, Λ_* seems to depend mainly on the bump height, for the fixed *Re* and *We* values. It has been also mentioned in [11], that heat transfer at the interface does not affect much the structure width. The dependence of Λ_* on bump height $H_{\max} - 1$ appeared to be not very strong either, the variation is just about 10% for the sufficiently large range $0.3 < H_{\max} - 1 < 0.8$.

Having the curves plotted in Fig. 10, allows to proceed to a comparison with experiment in three dimensions. The images of a film free surface from [11] obtained by optical Schlieren technique are depicted in Fig. 13. Corresponding (marked with the same letter) computed surface pictures are shown in Fig. 14 on the same scale. Time-dependent calculations for each *Ma* value have been performed in a region with $L_y = \Lambda_*$ till the saturation of the structure. The images in Fig. 14 are obtained picturing

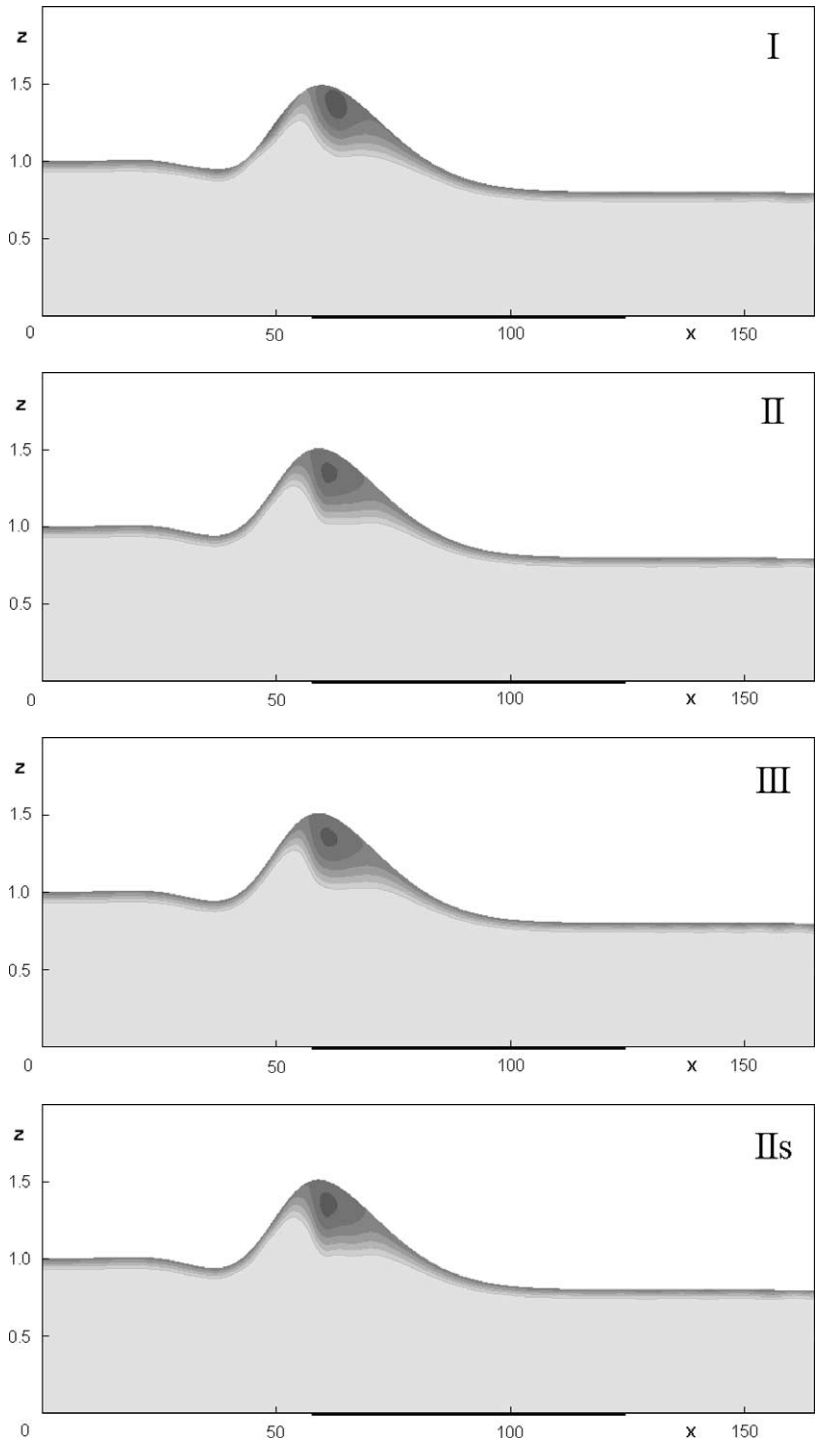

Fig. 8. Streamlines of steady state 2D flow at $Ma = 771$, $Bi = 0$ for different resolution: I – $m = 25$, $p = 2$, $N \approx 740$; II – $m = 50$, $p = 3$, $N \approx 2300$; III – $m = 100$, $p = 4$, $N \approx 8900$; IIs – the same resolution as II, but simplified strain rate tensor. The first level (the lowest contour) of dimensionless stream function corresponds to $\psi = 0.446$, the increment $\Delta\psi = 0.0146$. The bold line at the bottom designates a heater, $x_0 = 57.6$.

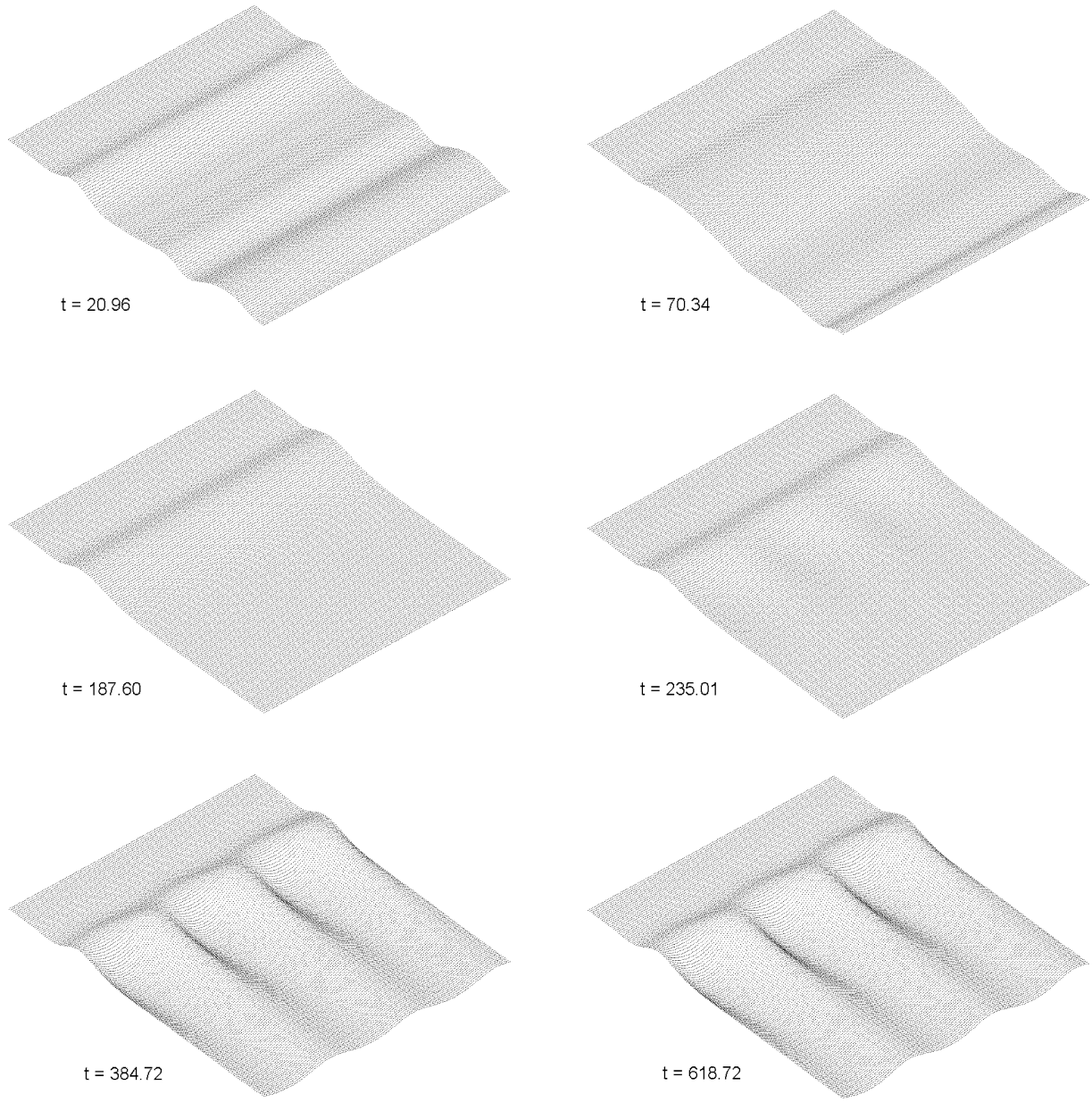

Fig. 9. Snapshots of the film surface at various dimensionless time levels for $Ma = 600,\ q_0 = 1.37\ \mathrm{W \cdot cm^{-2}},\ Bi = 0$.

grad $f(x, y)$. More exactly, in image (b) of Fig. 14 the grey level dependence on surface gradient is close to calibration curve from [7]. Therefore, flat free surface has a middle grey level, while positive and negative slopes along x are more dark and more light, respectively. This has been done in order to adjust the pictures scaling via a comparison of images (b) for experiment and calculation. As far as calibration curve for the 3D images is unknown, the black level in other pictures of Fig. 14 is proportional to $|\,\mathrm{grad}\, f(x, y)|$, starting with a light grey for a flat surface.

A comparison of Figs. 13 and 14 shows, first, a good agreement in threshold value of heat flux q for the instability to occur. This value appeared to be about $q = 1.08\ \mathrm{W \cdot cm^{-2}}$ in calculations, and it seems to be close to $q = 1.12\ \mathrm{W \cdot cm^{-2}}$ for the experiment, so the difference is just about 4%. Further, the agreement in structure width is also quite good, taking into account a spanwise inhomogeneity present in experiment. An increase in width of structure and a shift of the structure upstream with more intensive heating, are also captured in calculations, at least qualitatively. The spanwise inhomogeneity in Figs. 13 prevents one from making a more detailed comparison.

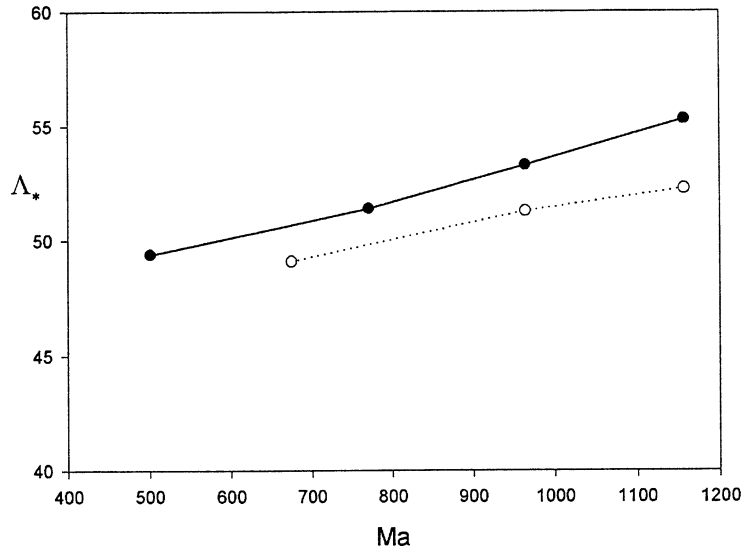

Fig. 10. The wavelength of the most unstable spanwise mode versus Marangoni number. Solid line – $Bi = 0$, dotted line – $Bi = 0.1$.

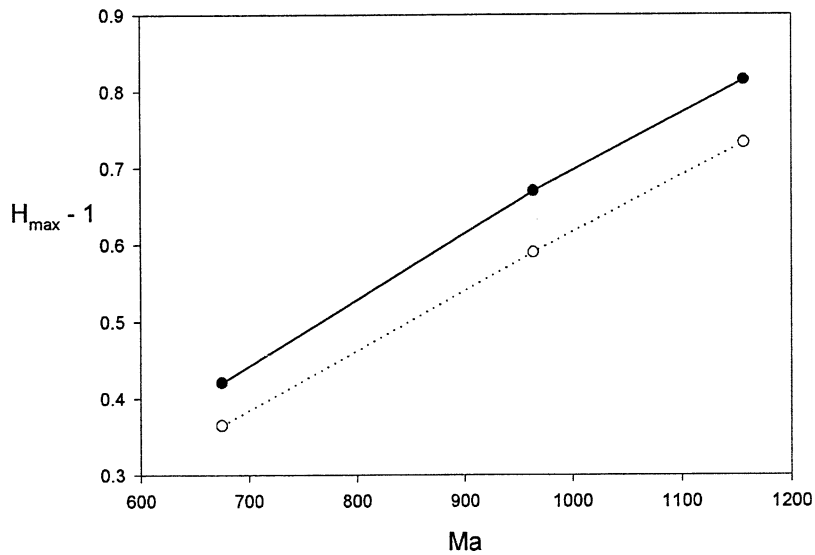

Fig. 11. The 2D bump height versus Marangoni number. Solid line – $Bi = 0$, dotted line – $Bi = 0.1$.

The longitudinal rolls seem to be more narrow and shaped more angular in experiment as compared with those computed, but it may be an optical illusion, as well. Any surface slope beyond some unknown limit (cut-off angle) should give a black color in Schlieren images (Fig. 13), in contrast to smooth grey scale in Fig. 14. Therefore, further investigation is needed here.

The main distinction between Figs. 13, 14 is the absence of small longitudinal rolls between the main ones in computed (e) and (f) images. It should be noted that free surface profile in some imaginary middle cross-section of the flow shown in Fig. 13(f) would be quite similar to the curves plotted in Fig. 4, so one may assume that small rolls formation is caused by secondary thermocapillary instability. The determinative factor for such an instability is a heat transfer at the free surface, which was neglected in our calculations. Fig. 15 presents a Biot number influence on the flow picture. It seems to confirm the above assumption. At least, the additional rolls appear between the main ones in a lower part of pictures, and this leads to a main rolls suppression, similar to what can be seen in Fig. 13. Some qualitative resemblance of the fine structure in heater region to that experimentally observed also can be seen. The main reason for the quantitative disagreement seems to be in capabilities of numerical computations.

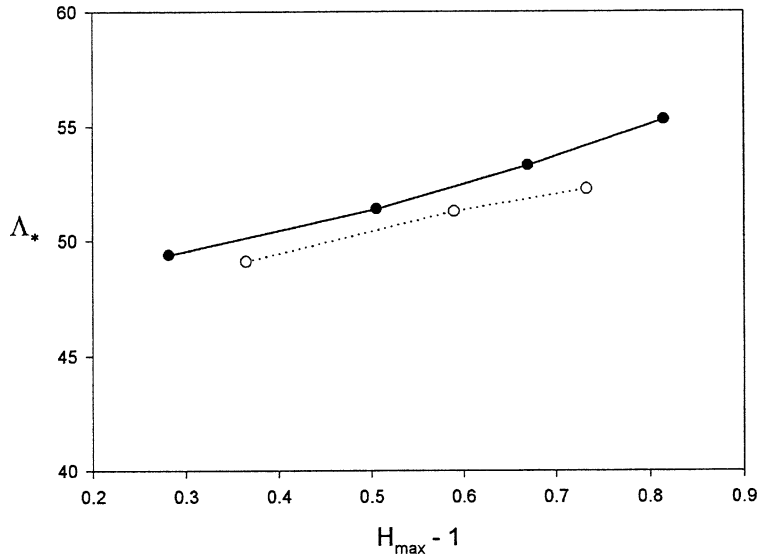

Fig. 12. The wavelength of the most unstable spanwise mode versus 2D bump height. Solid line – $Bi = 0$, dotted line – $Bi = 0.1$.

One can notice the small but sharp depressions of the film surface at the lower heater edge in (e2) and (e3) images of Fig. 15. The film rupture is occurred there. It should be noted that the method, in principle, allows to handle flows with variable connectivity. But the problem of relevant boundary conditions on moving contact line is known to be rather complicated, and it is a matter of future improvement of the method. Moreover, the rupture was not observed in experiment for these heat flux values, though some deformations of the rolls at the lower heater edge can be seen in Fig. 13. Therefore, either numerical resolution should be further increased, or *Bi* values shown in Fig. 15 are too large and should be diminished. But the latter leads to considerable slowing down the thermocapillary instability manifestation. For example, the linear growth rate of the most unstable disturbance, among spanwise thermocapillary modes in a vertical film flow, is proportional to Bi^2, when $Bi \ll 1$ [2]. Together with a necessity of taking fine enough spatial resolution, this leads, so far, to unacceptable computing time (see below). It's interesting, that the use of temperature profile (37), extended with a constant unit temperature up to the end of the domain, eliminates film rupture, as well as the intermediate rolls below the heater ((e4) in Fig. 15). The use of this profile avoids the abrupt change of temperature gradient at the low heater edge for $Bi \neq 0$. This shows, that rather fine peculiarities in bottom temperature distribution may happen to be of importance, and one cannot disregard the other possible reasons of discrepancy in fine structure, some of which are discussed in Section 7.

The image (e1) in Fig. 15 is pictured for the comparison with image (e) in Fig. 14, because Fig. 15 is obtained using more fine resolution $m = 50,\ n = 20$ (per one period of structure in spanwise direction), $p = 3,\ N \approx 150\,000$ (below is referred as resolution II), instead of the set of parameters $m = 25,\ n = 10,\ p = 2,\ N \approx 30\,000$ (resolution I) used in case corresponding to Fig. 14. The resolution I is the coarsest one used in 3D case, and it proved to be quite good if the free surface shape and some preliminary evaluation of velocity field for the main mode are of interest. Image (e1) looks very similar to (e) in Fig. 14. As for comparison of other quantities, the relative differences in $H_{\max}$, $U_{\max}$, $U_{\min}$ and q are 0.6%, 1.3%, 3.6% and 2.3%, respectively (see caption to Table 1 for an explanation). The typical run with the resolution I, starting from the undisturbed Nusselt solution and up to structure saturation takes less than half an hour on AMD Athlon XP2000 computer. But every further twofold resolution increase, results, in three dimensions, in about sixteen times greater time of computations.

Fig. 16 shows the isolines of surface elevation, temperature and streamwise covariant component of velocity at the surface $U_s = (u + f_x w)/U_0$ for the steady flow at $Ma = 675$. The velocity U_s is very close to streamwise velocity u/U_0, because the longitudinal surface gradient f_x and transverse velocity component w are both of the order of 10^{-1}. Fig. 17 demonstrates streamwise velocity in two longitudinal sections, and Fig. 18 displays velocity distribution in several cross-sections. These pictures reveal an interesting structure of the flow field. The spots of a strong reverse flow exist on the back side of a leading bump due to a thermocapillary forces (Figs. 16(c), 17(b), 18(a)). The presence of a reverse flow in a developed 3D structure has been recently evidenced experimentally [12]. The distance between the upstream edge of the heater and the stagnation point was found there to be about 1 mm, which quantitatively agrees with Fig. 16(c). The reverse flow magnitude has not been yet evaluated in experiments. The calculated minimum value of streamwise surface velocity U_s appeared to be -0.87 at $Ma = 675$, i.e., the magnitude of reverse flow is of the same order as that of inlet flow. This magnitude is two and a half times greater than that of reverse flow in 2D case shown in Fig. 8, though *Ma* value in 2D flow was about 15% greater (see Table 1). The maximum

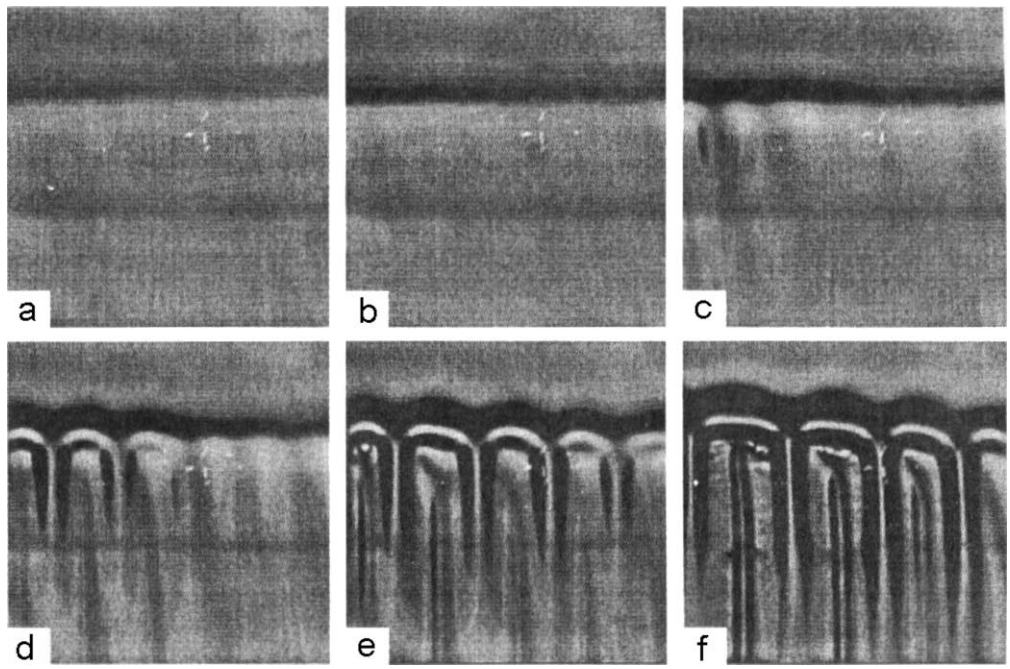

Fig. 13. The Schlieren images [11] of film surface at $Re = 0.5$ for different heat flux q values: a – $q = 0.3\ \mathrm{W \cdot cm^{-2}}$, b – $q = 0.63\ \mathrm{W \cdot cm^{-2}}$, c – $q = 1.12\ \mathrm{W \cdot cm^{-2}}$, d – $q = 1.21\ \mathrm{W \cdot cm^{-2}}$, e – $q = 1.5\ \mathrm{W \cdot cm^{-2}}$, f – $q = 2.11\ \mathrm{W \cdot cm^{-2}}$. Reproduced with the permission of the authors.

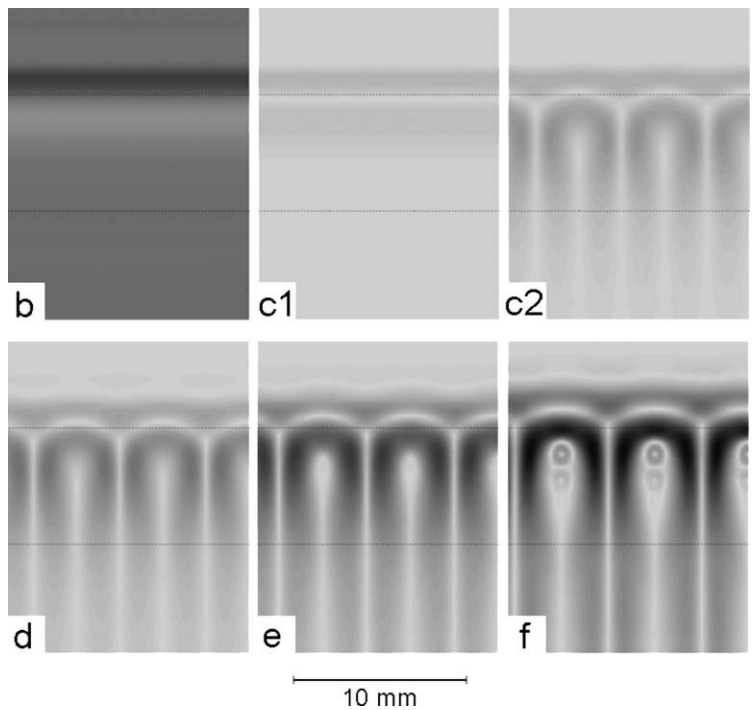

Fig. 14. The calculated pictures of film surface at $Re = 0.5$, $Bi = 0$ for different heat flux q values: b – $q = 0.63\ \mathrm{W \cdot cm^{-2}}$, $Ma = 273$; c1 – $q = 1.07\ \mathrm{W \cdot cm^{-2}}$, $Ma = 463$; c2 – $q = 1.12\ \mathrm{W \cdot cm^{-2}}$, $Ma = 486$; d – $q = 1.20\ \mathrm{W \cdot cm^{-2}}$, $Ma = 536$; e – $q = 1.46\ \mathrm{W \cdot cm^{-2}}$, $Ma = 675$; f – $q = 2.12\ \mathrm{W \cdot cm^{-2}}$, $Ma = 1022$. Dash lines show the heater region.

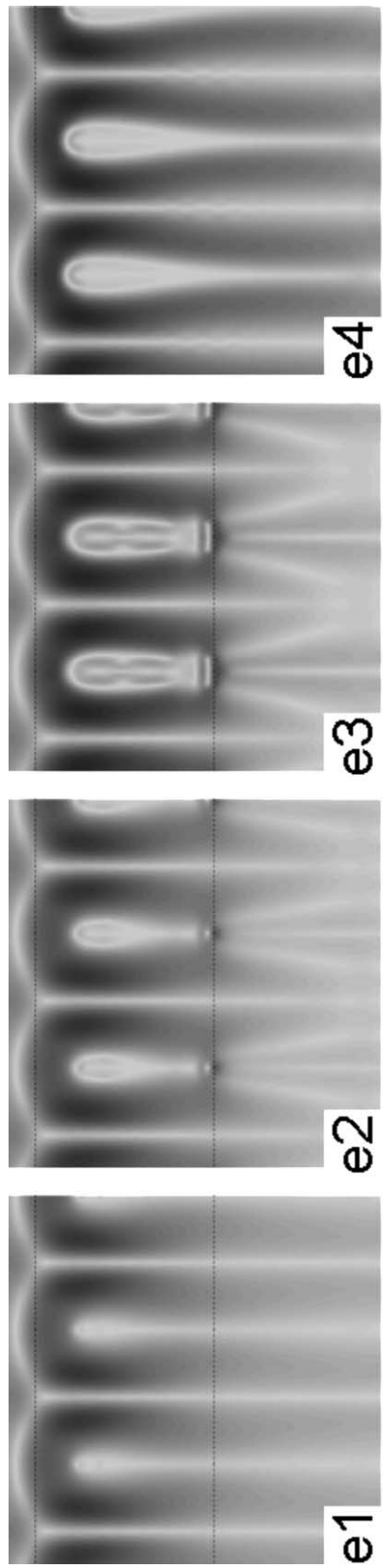

Fig. 15. The calculated pictures of film surface at $Re = 0.5$, $Ma = 675$, $t = 510$ for different Bi values: e1 – $Bi = 0$, $q = 1.43\ \mathrm{W \cdot cm^{-2}}$; e2 – $Bi = 0.03$, $q = 1.61\ \mathrm{W \cdot cm^{-2}}$; e3 – $Bi = 0.1$, $q = 2.08\ \mathrm{W \cdot cm^{-2}}$; e4 – $Bi = 0.1$, long heater (see text).

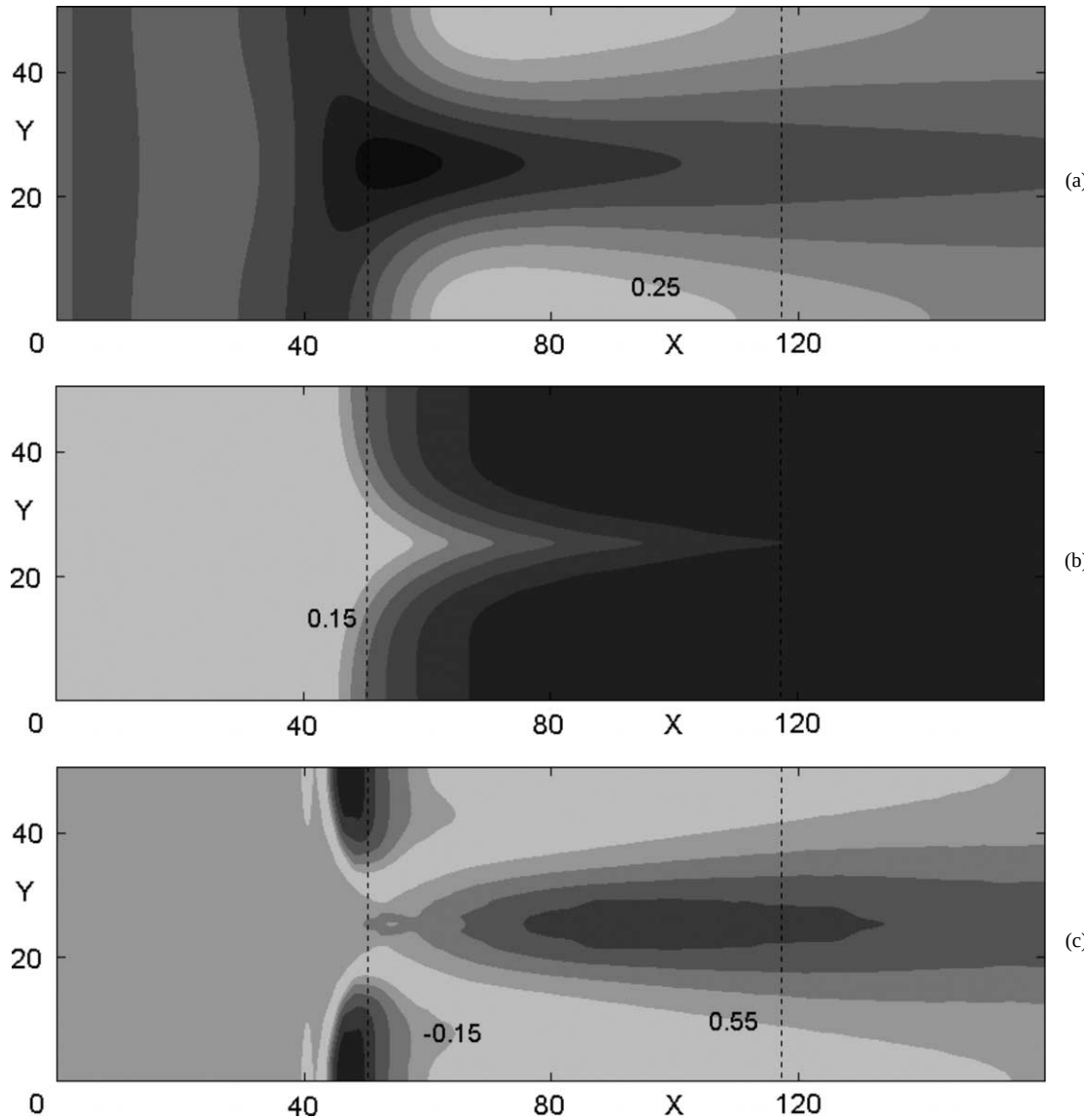

Fig. 16. Contour plots: (a) surface elevation f, (b) surface temperature T, (c) streamwise covariant component of velocity at the surface $U_s = (u + f_x w)/U_0$. The levels of the first isolines are given in pictures. The increments are: $\Delta f = 0.25,\ \Delta T = 0.15,\ \Delta U_s = 0.55$ (for $U_s > 0$) and $\Delta U_s = -0.15$ (for $U_s < 0$). In Figs. 16–19: $Ma = 675,\ Bi = 0,\ X_0 = 50.4,\ U_0 = 0.755$.

U_s value is 2.64 and it is reached around the crest of a longitudinal roll Fig. 16(c). The film in a trough is very thin, it's minimal thickness is 0.023, and the flow is nearly arrested there (Figs. 17, 18). Thus, the inlet stream splits up into longitudinal rolls or rivulets which flow out between vortices of thermocapillary nature. The increase in the flow rate downstream in a trough (Fig. 17(b)) is due to rivulets spreading.

The surface temperature field (Fig. 16(b)) shows that the liquid in a rivulet is colder than in a trough and this causes spanwise thermocapillary forces. Fig. 19(b) shows the strong contradirectional surface currents across the initial part of longitudinal roll crest, caused by surface temperature gradient (Fig. 19(a)). The maximum magnitude of spanwise surface velocity $V_s = (v + f_y w)/U_0$ is ± 1.6. And near the bottom the divergent stream appears (Fig. 18(b), $X = 66$). The heat transfer at the interface up to the $Bi = 0.1$ affects V_s field near the roll crest insignificantly.

The flow demonstrated in Figs. 16–18 was calculated with the resolution $m = 100,\ n = 40,\ p = 3, N \approx 600\,000$ (resolution III). It is about the finest resolution achievable on a desktop computer, and for steady state flows only, because the fields, obtained with more coarse resolution, can be used as a good initial guess. And this resolution was used mainly in

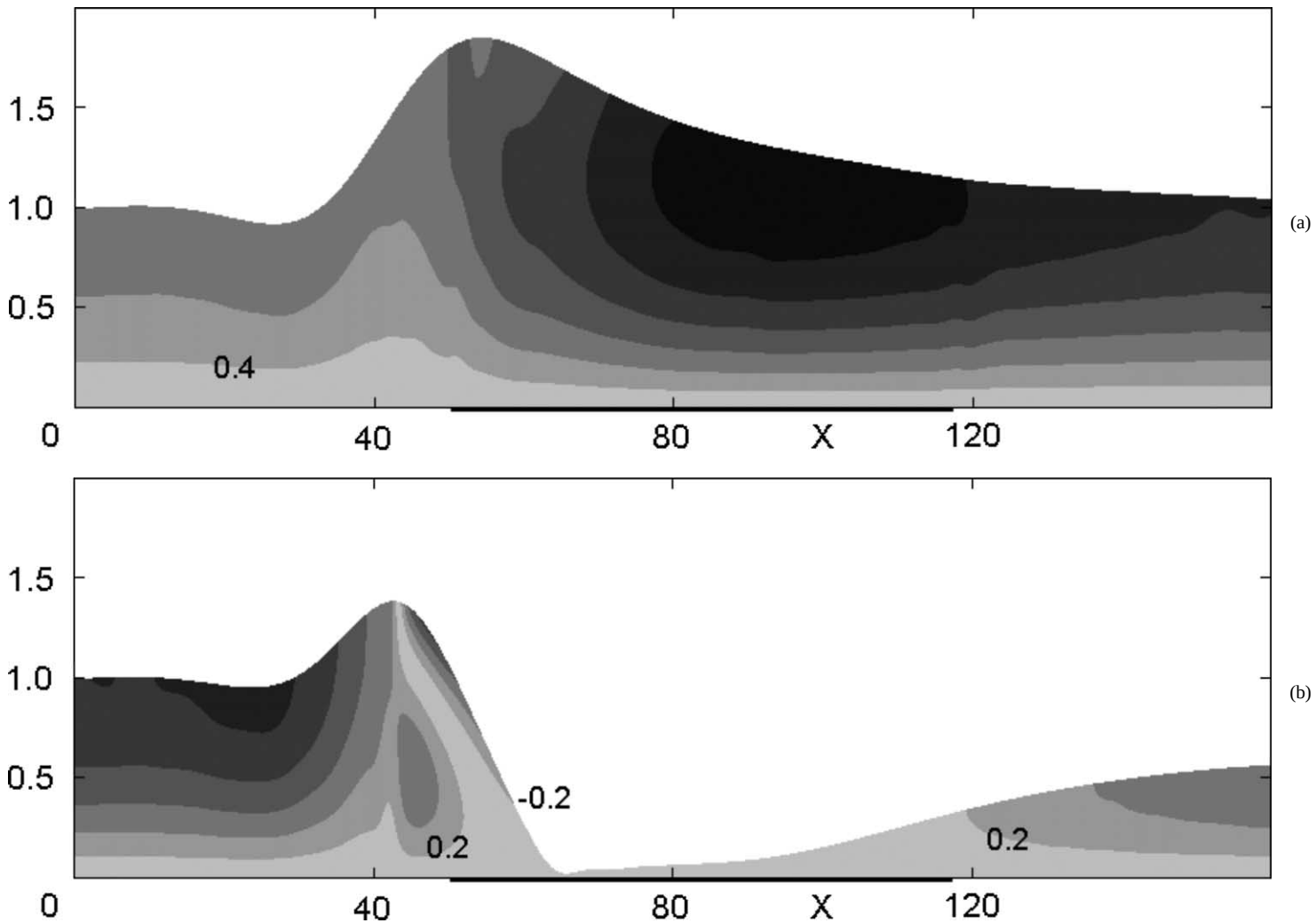

Fig. 17. Contour plots of streamwise velocity $U = u/U_0$ in two longitudinal sections: (a) $Y = 25.35$ (crest), increment $\Delta U = 0.4$; (b) $Y = 0$ (trough), increment $\Delta U = 0.2$, (-0.2 for the reverse flow).

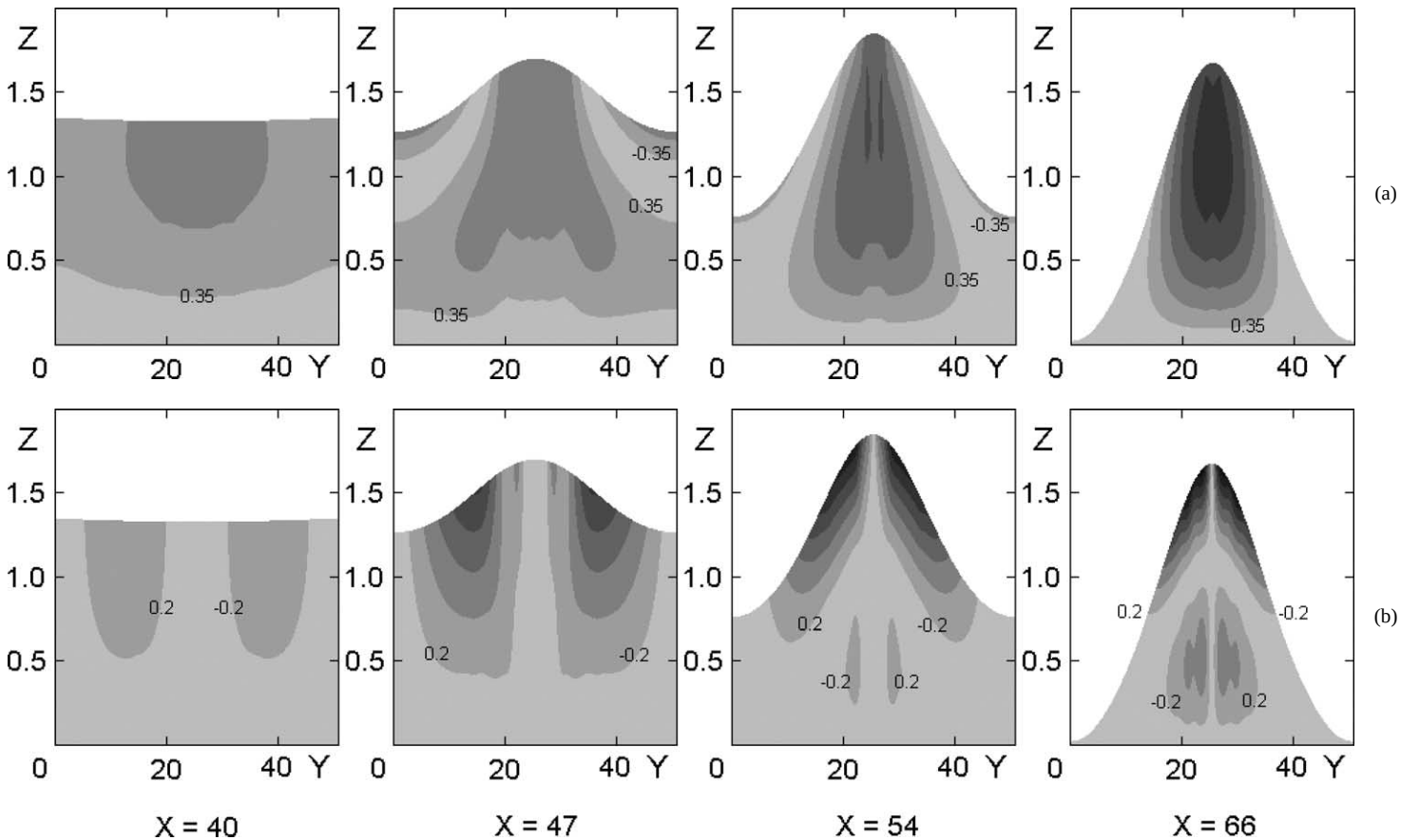

Fig. 18. Contour plots of streamwise velocity $U = u/U_0$ (a), and spanwise velocity $V = v/U_0$ (b) in several cross-sections (at X values shown below the figures). The absolute value of increments: (a) 0.35, (b) 0.2 (the sign is clear from pictures).

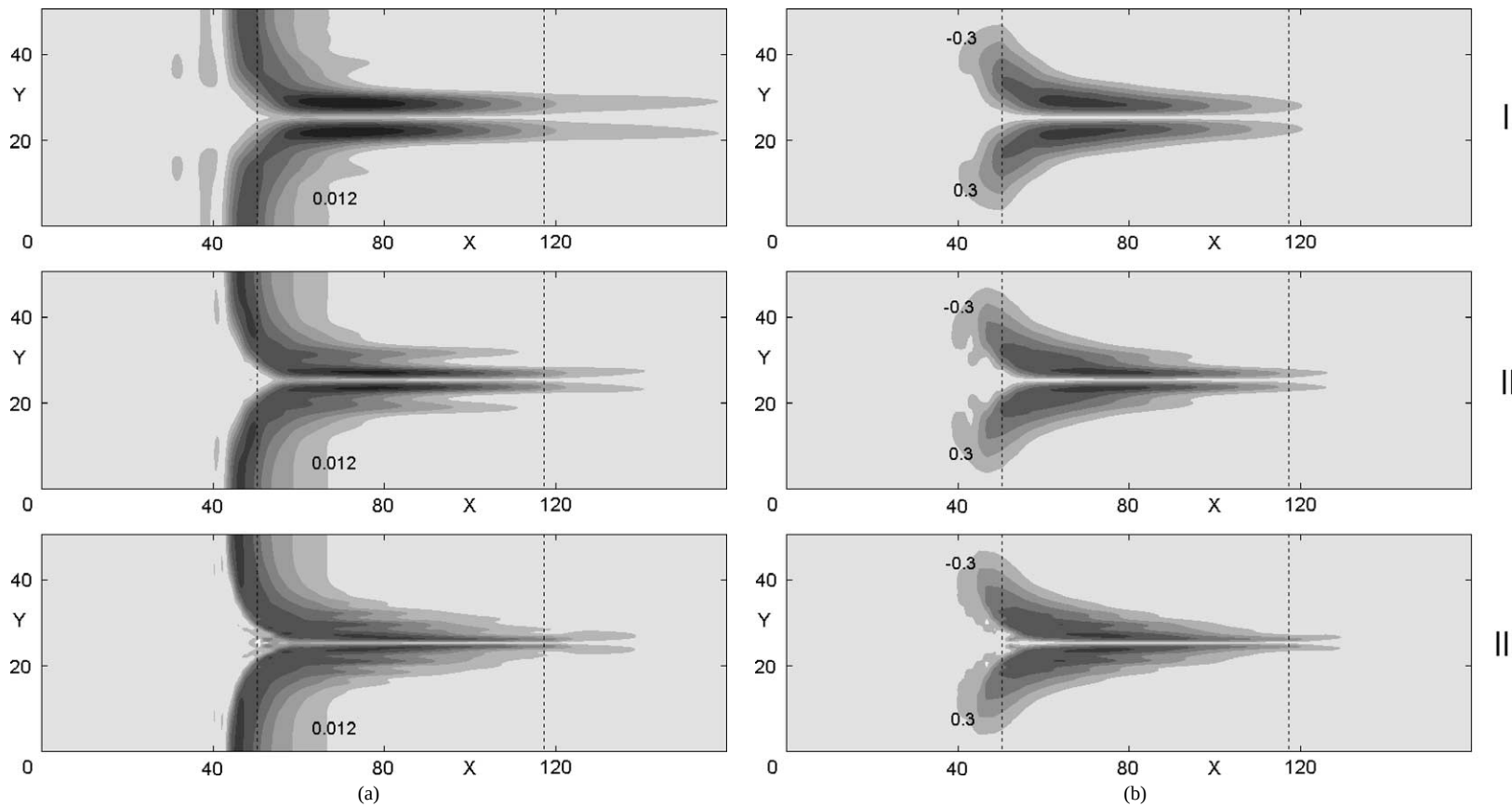

Fig. 19. Contour plots at three different resolutions: (a) surface temperature gradient (absolute value) $|\nabla_\Gamma T|$, increment 0.012; (b) spanwise covariant component of velocity at the surface $V_s = (v + f_y w)/U_0$, increment 0.3 (absolute value). Resolution: I – $m = 25,\ n = 10,\ p = 2,\ N \approx 30000$; II – $m = 50,\ n = 20,\ p = 3,\ N \approx 150000$; III – $m = 100, n = 40,\ p = 3,\ N \approx 600\,000$.

order to see where the surface temperature distribution converges to, and to clarify the reason of surface temperature gradient (and, hence, spanwise velocity) oscillations seen in Figs. 18, 19. The temperature isolines in Fig. 16(b) exhibit the sharp peaks at the crest of a rivulet, and therefore, the surface temperature gradient has an abrupt, almost step-wise within the limits of numerical resolution, change at the crest-line. It is not the case with a surface elevation gradient, which is smooth, and the reason seems to be in a large enough $Pr = 21.8$ value, which causes temperature inhomogeneities to be much thinner, than viscous boundary and inner layers. The fast change of surface temperature gradient, being not resolved well enough even for resolution III, causes the oscillations of $|\nabla_\Gamma T|$ and V_s. Nevertheless, computations with different resolution demonstrate close and converging results for the spanwise surface velocity field. The maximum value of dimensional surface temperature gradient is $13.5\ \mathrm{K}\cdot\mathrm{mm}^{-1}$, which is of the same order as observed [8] for the flow over 6.5×13 mm heater at $Re = 2$.

It should be mentioned here, that in spite of a stream being steady, the particles in calculations keep moving as well as fluid particles do in a real flow. The surface particles have small but finite dimensions, and therefore, the strong contradirectional surface currents cause cusps formation with time, if calculations are fully lagrangian. To avoid this, the method allows to implement the following simple procedure. Since at each time step one has a continuous velocity and temperature field, the particle redistribution can be easily made. As far as this procedure introduces some additional error, and can lead, in principle, to a violation of mass (momentum, energy) conservation, a special attention have been paid to it's application. Investigation in 2D and 3D cases showed that making a redistribution once over M steps, where $30 \lesssim M \lesssim 200$, allows to suppress cusps formation and does not lead to sensible interpolation errors. For example, in the 3D test problem, discussed in Section 5, the total fluid mass variation was less than 0.03%. Also, calculation of a steady state 3D flow with resolution I at $Ma = 600$ from $t = 600$ (the time of complete structure saturation) up to $t = 900$ (about 4000 steps, 130 redistributions) resulted in less than 0.1% relative variation of total fluid mass, streamwise momentum and kinetic energy.

As it was discussed above, the only period of structure is realized if computational domain width L_y is within some limits $L_1,\ L_2$. For the large enough Ma values, the interesting nonstationary transitional regimes are observed, when the domain width L_y is close to L_2. In Fig. 20 the snapshots of a film surface are presented, showing the oblique rivulets traveling across a computational domain. A quasistationary behaviour of the flow was mentioned to happen in experiment [11].

Finally, Fig. 21 depicts the mean heat transfer coefficient (Nusselt number $Nu = qH/kT_m$) versus Marangoni number for steady 2D, 3D and Nusselt flows. It shows, that the heat transfer from heater to fluid is noticeably inhibited due to a bump, and especially 3D structure, formation. A substantial decrease of heat transfer intensity, when strong deformations of the interface arose, was experimentally observed and described in [9,12]. Fig. 21 shows also, that solving a linear problem on heat transfer with the fixed Nusselt velocity field, as well as fully nonlinear but 2D problem, may result in quite substantial error in heat flux estimate at supercritical Ma values.

7. Conclusion and discussion

The present study has been aimed to simulate numerically the experimentally observed effect of 3D periodic structure formation in a falling film with local heating. The method of particles for incompressible fluid has been adapted in order to take into account viscous and surface tension forces. The particular case of a film flow at fixed $Re = 0.5$ over certain heater has been considered. The unknown temperature distribution on the heater has been reproduced through the comparison between calculated and measured free surface profiles at small heat flux values. The results described above show qualitative and quantitative agreement with observations [11] in several respects. The 3D instability takes place for the heat flux greater then some threshold, and this value is well predicted by the numerical model. The predicted characteristic width of a structure quantitatively agrees with the observed one, within the limits of observation accuracy. It is shown, that even large enough heat transfer at the interface slightly affects the structure width, that qualitatively agrees with observation experience. The more fine features, like an increase in width of structure and a shift of the latter upstream with more intensive heating, are also captured in calculations. The existence of some nonstationary regimes observed in experiment has been demonstrated, as well.

The calculations give an idea of interior flow structure, and some quantitative evaluations of local film thickness and velocity field, which seem to be difficult to measure. The nonzero heat transfer at the interface is shown to cause the additional rolls appearance between the main ones. The simulation revealed a strong contradirectional thermocapillary currents across the longitudinal roll crest, caused by spanwise temperature gradients. These spanwise thermocapillary forces seem to play a leading role in a periodic structure formation. Indeed, if a periodic external disturbance curves slightly a leading 2D bump in XY plane, then the spanwise surface temperature gradient immediately appears (at least, for the large enough Prandtl numbers), and thermocapillary forces tend to flatten the negative (upstream) part of a disturbance and to steepen the positive (downstream) one. This type of bump crest deformation one can see in the figures given above. As a result, the spanwise surface deformations become more acute, that amplifies spanwise surface temperature gradient. This simple consideration shows a possible mechanism of positive feedback necessary for any instability. It is important to mention also, that positive streamwise temperature gradient in a falling film should evidently provoke thermocapillary instability in the same way, as a heat transfer

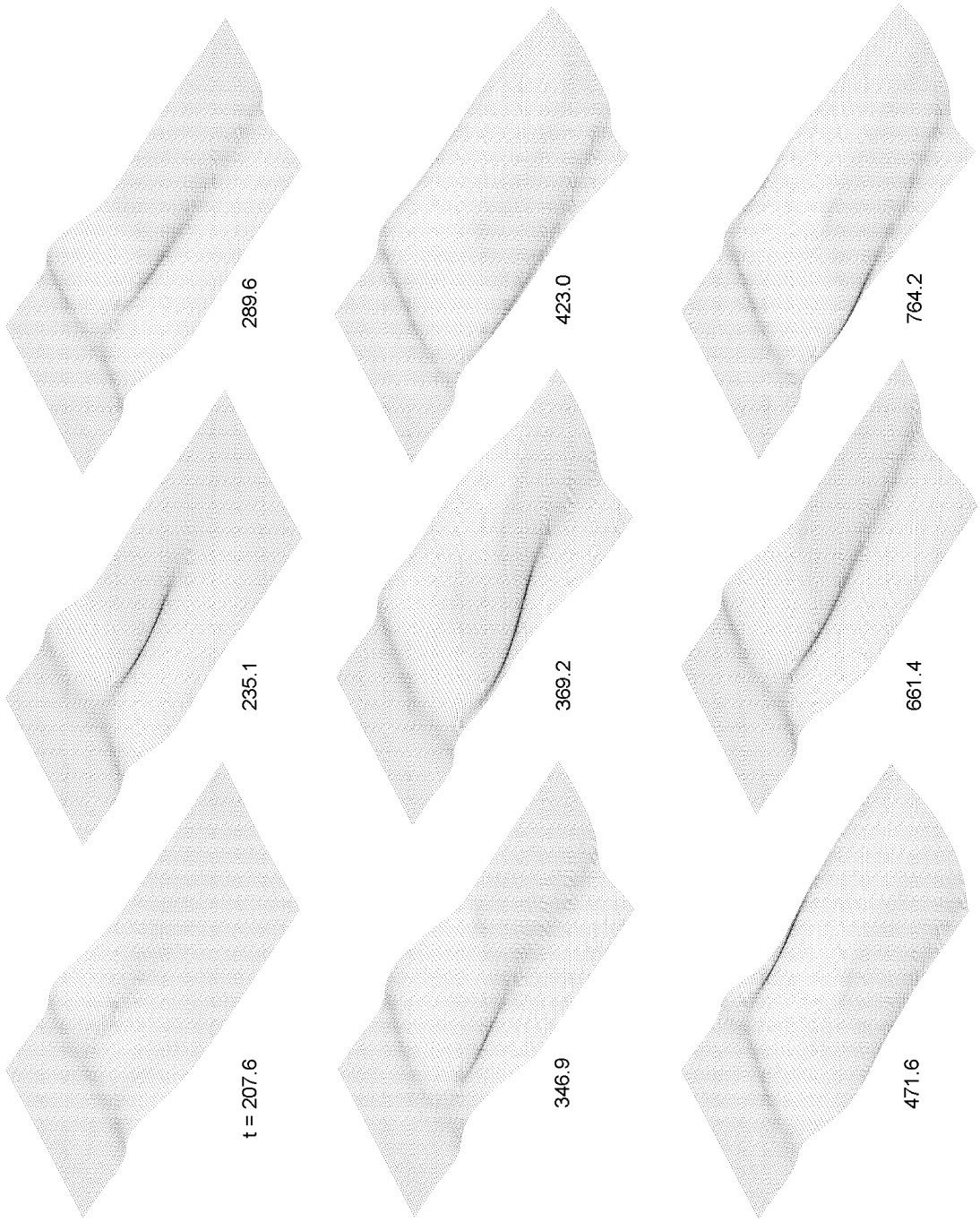

Fig. 20. Snapshots of the film surface at various dimensionless time levels for $Ma = 771$, $L_y = 75$, $Bi = 0$.

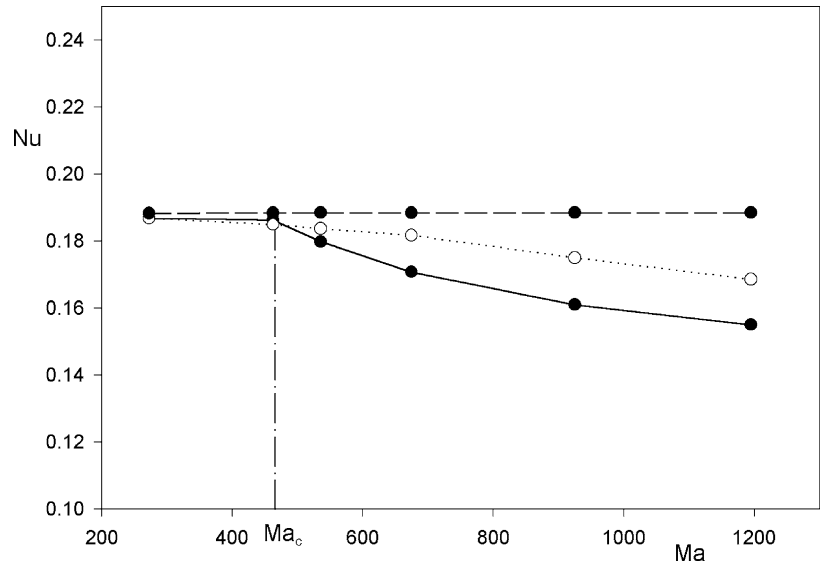

Fig. 21. Nusselt number $Nu = qH/kT_m$ versus Ma at $Bi = 0$. Solid line – 3D flow, dotted line – 2D flow, dash line – Nusselt flow. Critical Marangoni number value $Ma_c = 466$.

at the interface does (see, e.g., [4]). This may be the reason why Biot number in this particular problem with rather large base temperature gradient is not as important parameter, as it is in many other problems on thermocapillary instability.

Many interesting issues related to the problem are left open. First of all, the influence of Reynolds (or Galileo) and Weber numbers, which have been fixed throughout this study. The main problem here is the proper choice of bottom temperature distribution, which evidently must depend on these parameters if the investigation of phenomena observed in reality is intended. As discussed above, the most consistent approach would be, of course, to solve a fully coupled problem. However, the experience of present calculations gives a feeling that the heat transfer in substrate should be also taken into account. Keeping in mind some comparisons with certain experiment, this would require the knowledge of peculiar details of the experimental set-up, like specific heat and thermal conductivity of a substrate material, including that of, for example, epoxy resin and charcoal mixture, which was used in study [11] to mount the heater and to cover the surface of textolite plate. Therefore, we plan such a detailed future study in cooperation with the authors of experimental results cited above.

Further, the alcohol water solution is a mixture rather than a homogeneous liquid. Therefore, evaporation and "solutal" Marangoni effects, caused by gradients of surface concentration, can contribute to some discussed above discrepancies, like that between downstream branches of 2D bump profiles, or in mentioned above fine structure (small rivulets) at nonzero *Bi* values. All this needs further investigation both experimentally and theoretically.

Finally, the study of instability mechanism and bifurcation nature is of great interest and importance. All the more, the new interesting results on fingering instability of capillary ridge around a moving contact line, and on ridge stability for the flow over a step-down, have been recently obtained [34–36]. The capillary ridge around an obstacle seems to be a phenomenon quite close to the 2D bump around a "thermal obstacle". Still, the ridge appeared to be linearly stable, at least for the flow over step-down [36]. The main distinction between these two phenomena seems to be in destabilizing spanwise thermocapillary forces discussed above, but the accurate study and comparison is surely needed, including may be that for the ridges around the obstacles of other types. In [6], the study by Skotheim, Thiele and Scheid (to be published in J. Fluid Mech.) has been mentioned already, where the linear stability of 2D bump was investigated.

Acknowledgements

This work was partially supported by Siberian Division of Russian Academy of Science, integrated grants No. 1 and No. 5 (2000–2002) and also by Russian Foundation for Basic Research, grant 03-01-00218. The author is thankful to O.A. Kabov and E.A. Chinnov for the fruitful discussions and help, and also to the reviewers for their valuable remarks and suggestions.

Appendix A

Let there be surface Γ_b: $z = S(x, y)$, where S is a smooth function, and $\mathbf{u} = (u, v, w)$ is an arbitrary smooth divergence free field, vanishing on Γ_b. We are looking for the vector potential $\boldsymbol{\Theta} = (A, B, C)$, such that for $z > S(x, y)$

$$\begin{aligned} C_y - B_z &= u, \\ A_z - C_x &= v, \\ B_x - A_y &= w. \end{aligned} \tag{A.1}$$

Let $C \equiv 0$, A and B both vanish on Γ_b. Then, it follows from the two first equations (A.1)

$$B = -\int_S^z u \,\mathrm{d}z, \qquad A = \int_S^z v \,\mathrm{d}z. \tag{A.2}$$

Substituting functions (A.2) into the third equation (A.1) gives

$$B_x - A_y - w = -\int_S^z u_x \,\mathrm{d}z + uS_x|_S - \int_S^z v_y \,\mathrm{d}z + vS_y|_S - \int_S^z w_z \,\mathrm{d}z - w|_S = -\int_S^z (u_x + v_y + w_z)\,\mathrm{d}z \equiv 0$$

due to the continuity equation and boundary conditions. Thus, we have found vector potential $\boldsymbol{\Theta}$ with just two nonzero components, both vanishing on Γ_b together with their derivatives with respect to z.

References

[1] A. Oron, S.H. Davis, S.G. Bankoff, Long-scale evolution of thin liquid films, Rev. Modern Phys. 69 (3) (1997) 931–980.
[2] S.W. Joo, S.H. Davis, S.G. Bankoff, A mechanism for rivulet formation in heated falling films, J. Fluid Mech. 321 (1996) 279–298.
[3] M.K. Smith, S.H. Davis, Instabilities of dynamic thermocapillary liquid layers. Part 1. Convective instabilities, J. Fluid Mech. 132 (1983) 119–144.
[4] S. Miladinova, S. Slavtchev, G. Lebon, J.C. Legros, Long-wave instabilities of nonuniformly heated falling films, J. Fluid Mech. 453 (2002) 153–175.
[5] S. Miladinova, D. Staykova, G. Lebon, B. Scheid, Effect of nonuniform wall heating on the three-dimensional secondary instability of falling films, Acta Mech. 156 (2002) 79.
[6] B. Scheid, A. Oron, U. Thiele, J.C. Legros, Nonlinear evolution of nonuniformly heated falling liquid films, Phys. Fluids 14 (12) (2002) 4130–4151.
[7] B. Scheid, O.A. Kabov, C. Minetti, P. Colinet, J.C. Legros, Measurement of free surface deformation by reflectance-schlieren technique, in: E.W.P. Hahne, W. Heidemann, K. Spindler (Eds.), Proc. 3rd European Themal Sciences Conference, Vol. 1 (Heidelberg, Germany), Edizioni ETS, Pisa, Italy, 2000, pp. 651–657.
[8] O.A. Kabov, I.V. Marchuk, V.M. Chupin, Thermal imaging study of the liquid film flowing on vertical surface with local heat source, Russian J. Engrg. Thermophys 6 (2) (1996) 105–138.
[9] O.A. Kabov, E.A. Chinnov, Heat transfer from a local heat source to a subcooled falling liquid film evaporating in a vapor–gas medium, Russian J. Engrg. Thermophys 7 (1–2) (1997) 1–34.
[10] O.A. Kabov, Formation of regular structures in a falling liquid film upon local heating, Thermophys. Aeromech. 5 (1) (1998) 547–551.
[11] O.A. Kabov, J.C. Legros, I.V. Marchuk, B. Scheid, Deformation of the free surface in a moving locally-heated thin liquid layer, Izv. Ross. Akademii Nauk Mekh. Zhidk. Gaza 3 (2001) 200–208;
English translation: O.A. Kabov, J.-C. Legros, I.V. Marchuk, B. Scheid, Deformation of the free surface in a moving locally-heated thin liquid layer, Fluid Dynamics 36 (3) (2001) 521–528.
[12] O.A. Kabov, B. Scheid, I.A. Sharina, J.C. Legros, Heat transfer and rivulet structures formation in a falling thin liquid film locally heated, Int. J. Therm. Sci. 41 (2002) 664–672.
[13] I.V. Marchuk, O.A. Kabov, Numerical modelling of thermocapillary reverse flow in thin liquid films under local heating, Russian J. Engrg. Thermophys. 8 (1–4) (1998) 17–46.
[14] V.V. Kuznetsov, Dynamics of locally heated liquid films, Russian J. Engrg. Thermophys. 10 (2) (2000) 107–120.
[15] O.A. Kabov, B. Scheid, V.V. Kuznetsov, I.O. Kabova, J.C. Legros, Free surface deformation in a locally heated falling thin liquid film with the temperature dependent viscosity, in: J. Taine (Ed.), Heat Transfer 2002, Vol. 2, Proc. 12th Int. Heat Transfer Conference, Grenoble, France, August 18–23, 2002, pp. 675–680.
[16] T.R. Salamon, R.C. Armstrong, R.A. Brown, Travelling waves on vertical films: Numerical analysis using the finite element method, Phys. Fluids 6 (1994) 2202–2220.
[17] B. Ramaswamy, S. Chippada, S.W. Joo, A full-scale numerical study of interfacial instabilities in thin-film flows, J. Fluid Mech. 325 (1996) 163–194.

[18] S. Krishnamoorthy, B. Ramaswamy, S.W. Joo, Spontaneous rupture of thin liquid films due to thermocapillarity; A full-scale direct numerical simulation, Phys. Fluids 7 (1995) 2291–2293.
[19] B. Ramaswamy, S. Krishnamoorthy, S.W. Joo, Three-dimensional simulation of instabilities and rivulet formation in heated falling films, J. Comput. Phys. 131 (1997) 70–88.
[20] A.M. Frank, E.I. Ogorodnikov, Method of particles for an incompressible fluid, Soviet Phys. Dokl. 37 (1992) 489–491.
[21] A.M. Frank, Discrete Models of Incompressible Fluid, Fizmatlit, Moscow, 2001 (in Russian).
[22] A.M. Frank, Particle method for water waves simulation, in: G. Cohen (Ed.), Proc. 3rd Int. Conf. on Mathematical and Numerical Aspects of Wave Propagation, Mandelieu-la-Napoule, SIAM–INRIA, France, 1995, pp. 96–103.
[23] V.K. Andreev, A.M. Frank, Stability of Couette flow of an ideal fluid with free boundaries, J. Appl. Mech. Techn. Phys. 39 (5) (1998) 738–743.
[24] A.M. Frank, Numerical simulation of liquid jet holding a cylinder, Int. J. Comput. Fluid Dynamics 10 (1998) 315–320.
[25] A.M. Frank, Numerical simulation of holding a ball by a fluid jet, Dokl. Phys. 44 (3) (1999) 196–199.
[26] E.V. Ovchinnikova, A.M. Frank, On the convergence for the method of particles for viscous incompressible fluid, in press.
[27] G. Strang, G.J. Fix, An Analysis of the Finite Element Method, Prentice-Hall, Englewood Cliffs, 1973.
[28] P. Appel, Theoretical Mechanics, Fizmatgiz, Moscow, 1960 (in Russian).
[29] R. Temam, Navier–Stokes Equations, Theory and Numerical Analysis, North-Holland, Amsterdam, 1979.
[30] P.L. Kapitza, S.P. Kapitza, Wave flow of thin layers of a viscous fluid: III. Experimental study of undulatory flow regime, Zh. Exper. Teoret. Fiz. 19 (1949) 105–120.
[31] O.A. Kabov, Capillary effects influence on vapor liquid film condensation and heat transfer in falling liquid film, Dr. Sci. thesis, Institute of Thermophysics SB RAS, Novosibirsk, 1999 (in Russian).
[32] I.V. Marchuk, O.A. Kabov, Numerical simulation of heat transfer in a falling liquid film with allowance for heat conduction in heaters, Russian J. Engrg. Thermophys. 10 (2) (2000) 147–165.
[33] E.A. Chinnov, O.A. Kabov, I.V. Marchuk, D.V. Zaitsev, Heat transfer and breakdown of sub-cooled falling liquid film on a vertical middle size heater, Int. J. Heat Technology 20 (1) (2002) 69–78.
[34] M. Eres, L. Schwartz, R. Roy, Fingering phenomena for driven coating films, Phys. Fluids 12 (6) (2000) 1278–1295.
[35] S. Kalliadasis, Nonlinear instability of a contact line driven by gravity, J. Fluid Mech. 413 (2000) 355–378.
[36] S. Kalliadasis, G.M. Homsy, Stability of free-surface thin-film flows over topography, J. Fluid Mech. 448 (2001) 387–410.